

VAE-SNE: a deep generative model for simultaneous dimensionality reduction and clustering

Jacob M. Graving^{1,2,3,*}, and Iain D. Couzin^{1,2,3,*}

1 Department of Collective Behaviour, Max Planck Institute of Animal Behavior, 78464 Konstanz, Germany

2 Centre for the Advanced Study of Collective Behaviour, University of Konstanz, 78464 Konstanz, Germany

3 Department of Biology, University of Konstanz, 78464 Konstanz, Germany

*e-mail: jgraving@gmail.com; icouzin@ab.mpg.de

keywords: representation learning, pose estimation, animal behavior, neuroscience, *Drosophila*, single-cell analysis, natural images

1 Abstract

Scientific datasets are growing rapidly in scale and complexity. Consequently, the task of understanding these data to answer scientific questions increasingly requires the use of compression algorithms that reduce dimensionality by combining correlated features and cluster similar observations to summarize large datasets. Here we introduce a method for both dimension reduction and clustering called VAE-SNE (variational autoencoder stochastic neighbor embedding). Our model combines elements from deep learning, probabilistic inference, and manifold learning to produce interpretable compressed representations while also readily scaling to tens-of-millions of observations. Unlike existing methods, VAE-SNE simultaneously compresses high-dimensional data and automatically learns a distribution of clusters within the data – without the need to manually select the number of clusters. This naturally creates a multi-scale representation, which makes it straightforward to generate coarse-grained descriptions for large subsets of related observations and select specific regions of interest for further analysis. VAE-SNE can also quickly and easily embed new samples, detect outliers, and can be optimized with small batches of data, which makes it possible to compress datasets that are otherwise too large to fit into memory. We evaluate VAE-SNE as a general purpose method for dimensionality reduction by applying it to multiple real-world datasets and by comparing its performance with existing methods for dimensionality reduction. We find that VAE-SNE produces high-quality compressed representations with results that are on par with existing nonlinear dimensionality reduction algorithms. As a practical example, we demonstrate how the cluster distribution learned by VAE-SNE can be used for unsupervised action recognition to detect and classify repeated motifs of stereotyped behavior in high-dimensional timeseries data. Finally, we also introduce variants of VAE-SNE for embedding data in polar (spherical) coordinates and for embedding image data from raw pixels. VAE-SNE is a robust, feature-rich, and scalable method with broad applicability to a range of datasets in the life sciences and beyond.

1 Introduction

Modern scientific research generates large, high-resolution datasets that are complex and high-dimensional, where a single observation from an experimental system can contain measurements describing hundreds, or thousands, of features. For example, neuroscientists measure electrical activity across thousands of individual neurons simultaneously (Jun et al., 2017; Stringer et al., 2019a,b) – even across the entire brain (Ahrens et al., 2012, 2013); cell biologists and bioinformaticians routinely sequence the transcriptome for thousands of genes across large populations of single cells (Samusik et al., 2016; La Manno et al., 2018; Becht et al., 2019; Linderman et al., 2019); behavioral scientists measure the high-dimensional body posture dynamics of animals and humans (Stephens et al., 2008, 2011; Kain et al., 2013; Berman et al., 2014; Wiltshchko et al., 2015; Klibaite et al., 2017; Costa et al., 2019;

34 Cande et al., 2018; Mathis et al., 2018; Chambers et al., 2019; Günel et al., 2019; Graving et al., 2019;
35 Klibaite and Shaevitz, 2019; Nath et al., 2019; Pereira et al., 2019; Bala et al., 2020; Ebbesen and Froemke,
36 2020; Karashchuk et al., 2020); and evolutionary ecologists measure complex morphological patterns
37 across sizeable collections of animal specimens (Cuthill et al., 2017, 2019; Ezray et al., 2019; Wham et al.,
38 2019; Zhang et al., 2019). While there are many benefits to measuring real-world systems accurately and
39 completely for answering scientific questions, this added complexity poses problems for conventional
40 data analysis methods – especially those commonly used in the life sciences, like linear models (Bolker
41 et al., 2009) – that are designed for small, low-dimensional datasets and typically rely on simplified
42 models with strong, often unrealistic, assumptions for making statistical inferences.

43 To deal with the complexity of modern data, researchers in many fields have begun to use
44 machine-learning methods known as *dimensionality reduction* and *clustering* to help interpret large,
45 high-dimensional datasets. These algorithms distill correlated features down to a smaller set of
46 components (dimensionality reduction) or group large subsets of observations into a smaller set of
47 classes based on similarity (clustering). Together these methods offer scientists a way to *compress*
48 data, where compression is typically performed with the goal of reducing the size and complexity of a
49 dataset while making only minimal, or very general, a priori assumptions about the true distribution of the
50 data. Because these algorithms derive their compressed representations directly from the structure of
51 the data itself, without human supervision, they are typically known as *unsupervised learning* algorithms.

52 Across many scientific disciplines, unsupervised algorithms are rapidly becoming a commonly-used
53 tool for visualizing and interpreting high-dimensional data distributions as well as summarizing large
54 datasets with coarse-grained descriptions and identifying specific subpopulations and regions of
55 interest within the data for further downstream analysis. Researchers have applied these methods to
56 demonstrate how the brain organizes behavior (Stephens et al., 2008, 2011; Brown et al., 2013; Wiltshcko
57 et al., 2015; Berman et al., 2016; Billings et al., 2017; Cande et al., 2018; Markowitz et al., 2018; Costa et al.,
58 2019; Stringer et al., 2019a,b); describe how cells grow and develop over time (La Manno et al., 2018);
59 document new and rare types of cells (Grün et al., 2015; Linderman et al., 2019); gain insights into cancer
60 treatment (Tirosh et al., 2016); and reveal fundamental principles of evolution (Cuthill et al., 2019; Ezray
61 et al., 2019; Wham et al., 2019). Therefore, as scientists begin to regularly rely on these algorithms for
62 analyzing complex datasets, the task of ensuring the quality, robustness, and utility of the compressed
63 representations they produce is an issue of considerable importance – as is the ability to scale these
64 methods to increasingly large datasets.

65 While existing methods for dimension reduction produce high-quality compressed representations
66 (Becht et al., 2019; Kobak and Linderman, 2019), they typically lack features for identifying groups of
67 similar data (i.e., learned clusters; but see Pezzotti et al. 2016; Robinson and Pierce-Hoffman 2020), and
68 despite much progress to improve scalability of existing algorithms (Linderman et al., 2017; McInnes
69 et al., 2018; Linderman et al., 2019), some of the most widely-used methods are still limited in their ability
70 to scale beyond a few million observations without specialized, high-performance hardware – especially
71 in the case of large, out-of-core datasets that cannot fit into memory. Recent applications of deep
72 learning (Goodfellow et al., 2016), and deep generative models in particular (Appendix A.1; Kingma and
73 Welling 2013; Rezende et al. 2014), have begun to address these issues (Ding et al., 2018; Szubert et al.,
74 2019; Ding and Regev, 2019). Nevertheless, even with the low memory and computational cost of deep
75 learning methods that can be trained with small batches of data on consumer-grade hardware, these
76 new algorithms are still significantly slower to fit to data than more popular methods because they
77 require costly nearest neighbor or pairwise distance calculations (Becht et al., 2019; Ding et al., 2018;
78 Szubert et al., 2019). The majority of these methods also do not provide any built-in mechanism for
79 detecting outliers, which could potentially bias any downstream results and cause statistical errors
80 when testing hypotheses.

81 There has also been a flurry of recent work on advanced methods for clustering data (e.g., Campello
82 et al. 2013; Jiang et al. 2016; Xie et al. 2016; Guo et al. 2017; McInnes et al. 2017; Fogel et al. 2019; Yang
83 et al. 2019; Robinson and Pierce-Hoffman 2020; and numerous others), including efficient methods that
84 rely on deep learning and deep generative models. However, the vast majority of these methods impose
85 strong assumptions about the shape of the clusters and require the user to manually select the number

86 of clusters fitted to the data — or, alternatively, involve complex computations that do not scale well to
87 large datasets. Determining how many clusters to fit is typically a non-trivial, unintuitive, and
88 computationally-intensive task for datasets where the number of clusters is not known a priori (Milligan
89 and Cooper, 1985; Pham et al., 2005; Fang and Wang, 2012; Todd et al., 2017). Many recently proposed
90 clustering algorithms are also only evaluated with relatively small “toy” datasets, such as the MNIST
91 handwritten digit database (LeCun et al., 2010), where the data typically have very little noise, no outliers,
92 and the number of clusters is often known a priori. This lack of rigorous real-world assessment casts
93 doubt on the practical utility of these algorithms in cases where datasets have a large number of
94 observations, are naturally noisy or contain outliers, and the number of clusters is unknown, such as
95 those commonly used in the natural sciences.

96 Here we aim to address many of the limitations outlined above and unify some of the key
97 methodological concepts from previous work into a single modeling framework. To accomplish this, we
98 introduce a deep generative model for both dimensionality reduction and clustering. We then compare
99 our model with existing methods for dimensionality reduction, and importantly, to ensure that it has
100 practical utility, we demonstrate the application of our method using empirical examples with real-world
101 data from multiple domains. In comparison to existing dimension reduction methods, our proposed
102 method produces low-dimensional data representations with similar, or better, quality while also offering
103 several key improvements. Notably, our approach provides the ability to scale to datasets containing
104 tens-of-millions of observations without specialized, high-performance hardware and automatically
105 learns an interpretable cluster distribution from the data without any manual tuning or expensive
106 computations to determine the number of clusters. Together these results demonstrate that our
107 proposed method is a robust, feature-rich, and scalable tool for data analysis and is widely-applicable to
108 a variety of tasks.

109 2 Results

110 We make three main contributions in this paper: (1) First, we introduce a deep generative model for both
111 dimensionality reduction and clustering called variational autoencoder stochastic neighbor embedding
112 (VAE-SNE; Fig. 1; Methods). VAE-SNE can produce a variety of different compressed representations and
113 readily scales to out-of-core datasets with tens-of-millions of observations. Our model builds on
114 numerous ideas from past work by synthesizing methods from a class of generative models known as
115 variational autoencoders (VAEs; Kingma and Welling 2013), the popular dimensionality reduction
116 algorithm (t -distributed) stochastic neighbor embedding (SNE/ t -SNE; Hinton and Roweis 2003; van der
117 Maaten and Hinton 2008) and its many extensions (van der Maaten, 2009; Wang and Wang, 2016; Chien
118 and Hsu, 2017; Ding et al., 2018), as well as recent advances in variational inference (Kingma et al., 2014;
119 Burda et al., 2015; Dilokthanakul et al., 2016; Cremer et al., 2017; Tomczak and Welling, 2017) and
120 clustering methods (Todd et al., 2017). (2) Second, we apply VAE-SNE, and a variety of other popular
121 dimensionality reduction methods, to compress real-world datasets from different domains (Fig. 2). We
122 then quantitatively assess how each algorithm performs in preserving important aspects of the data —
123 including information about local, global, and temporal structure. We also assess generalization to new,
124 out-of-sample data and compare processing speeds for each algorithm. Additionally, we show how the
125 likelihood score produced by VAE-SNE can be used to detect outliers when embedding out-of-sample
126 data. (3) Third, we show how VAE-SNE can be used to automatically cluster large datasets into a small
127 set of interpretable classes. As a practical example, we apply VAE-SNE to a dataset of 21.1 million
128 observations describing the high-dimensional body posture dynamics of a commonly-used model
129 organism — the fruit fly (*Drosophila melanogaster*) — to automatically discretize these data into motifs
130 of stereotyped behavior for further analysis (Fig. 3; Berman et al. 2014; Pereira et al. 2019). These results
131 illustrate how VAE-SNE can be used as a type of automated ethogram for describing the full behavioral
132 repertoire of animals (reviewed by Anderson and Perona 2014; Berman 2018; Brown and De Bivort 2018;
133 Datta et al. 2019), while also providing several advantages over existing methods for this task.

134 Our approach (Fig. 1; Methods) builds on VAEs as a base model for performing dimensionality

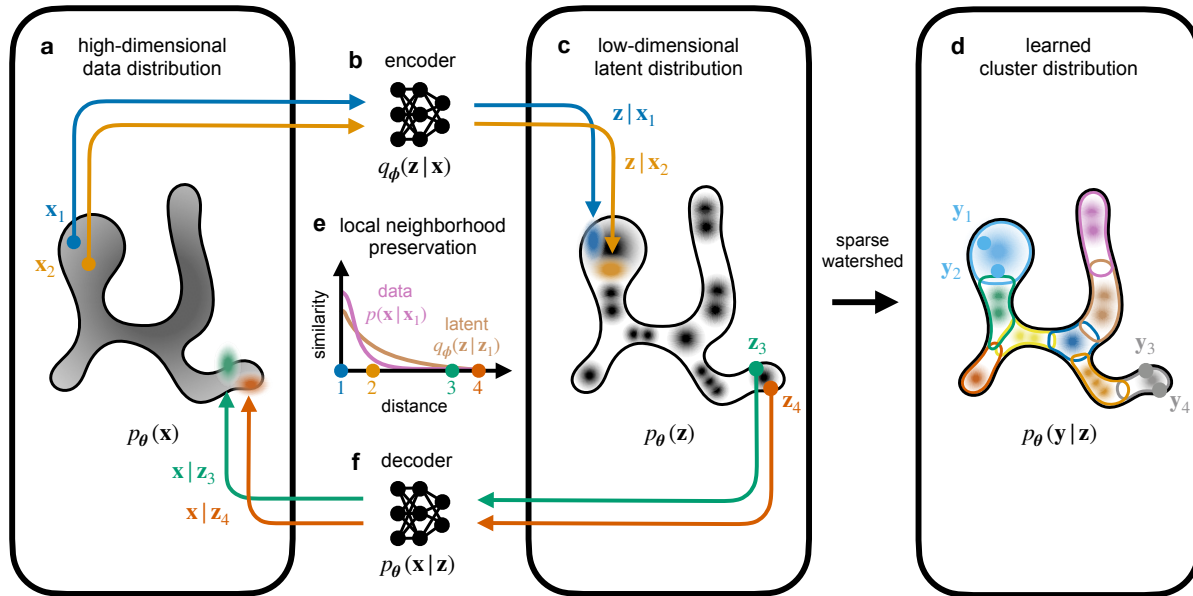


Figure 1. Overview of the VAE-SNE model. **a-f**, Observed samples from a high-dimensional data distribution $\mathbf{x} \sim p(\mathbf{x})$ (**a**) are probabilistically embedded (**b**) into a low-dimensional latent distribution $p_{\theta}(\mathbf{z})$ (**c**) using an encoder deep neural network $\text{DNN}_{\phi} : \mathbf{x} \rightarrow \mathbf{z}$ to generate an approximate latent posterior distribution $q_{\phi}(\mathbf{z}|\mathbf{x})$. Samples from the latent distribution $\mathbf{z} \sim q_{\phi}(\mathbf{z}|\mathbf{x})$ or $\mathbf{z} \sim p_{\theta}(\mathbf{z})$ (**c**) are then transformed (**f**) using a generative decoder deep neural network $\text{DNN}_{\theta} : \mathbf{z} \rightarrow \mathbf{x}$ to probabilistically reconstruct the high-dimensional data distribution $p_{\theta}(\mathbf{x}|\mathbf{z})$. Given a set of observed high-dimensional data $\{\mathbf{x}_1, \mathbf{x}_2, \dots, \mathbf{x}_N\}$ the model parameters for the encoder and decoder $\{\theta, \phi\}$ are optimized so that the approximate posterior for the encoder matches the true posterior from the generative decoder as best as possible, or $q_{\phi}(\mathbf{z}|\mathbf{x}) \approx p_{\theta}(\mathbf{z}|\mathbf{x})$, which then creates a functional mapping between the high-dimensional and low-dimensional distributions. To improve local structure preservation during optimization, pairwise distances between vectors in the high-dimensional and low-dimensional space are optimized using pairwise similarity kernels (**e**), a probability density function of distance, so that the local neighborhoods around each observation match as best as possible, or $p(\mathbf{x}|\mathbf{x}_i) \approx q_{\phi}(\mathbf{z}|\mathbf{z}_i)$. This preferentially weights the preservation of local neighborhoods over global relationships by assigning more probability mass to nearby neighbors during optimization. The prior for the latent distribution $p_{\theta}(\mathbf{z})$ is also a learned Gaussian mixture distribution (**c**) that is jointly optimized with the encoder and decoder to fit the observed data and can be used to cluster the latent distribution (**d**) into a small set of discrete classes $p_{\theta}(\mathbf{y}|\mathbf{z})$ – where highly-overlapping modes (mixture components) within the distribution are automatically merged into the same class label using sparse watershed assignment (Methods; Todd et al. 2017)

135 reduction (Appendix A.1), which, like other types of autoencoders (Hinton and Salakhutdinov, 2006),
136 model high-dimensional data using two deep neural networks: one to encode data to a compressed
137 latent representation, and another to decode the latent vectors and reconstruct the data. However, VAEs
138 are distinct from other autoencoders in that the encoder is used to parameterize continuous
139 distributions of latent vectors – from which latent vectors are then probabilistically sampled – rather
140 than embedding each high-dimensional observation as a single point in the latent space. This type of
141 model offers an attractive dimensionality reduction framework because the objective function (Appendix
142 A.2) naturally imparts a trade-off between the complexity of the encoded description and the overall
143 accuracy of the decoded reconstruction (Aleml et al., 2016). However, these models suffer from multiple
144 long-standing issues including a phenomenon known as *posterior collapse* (Aleml et al., 2017; Dieng
145 et al., 2019a) where the latent coordinate space becomes arbitrarily organized and no longer preserves
146 any statistical features of the high-dimensional data distribution. There has been a string of recent work
147 to address these issues including some relatively straightforward solutions (Higgins et al., 2016; Dieng
148 et al., 2019a) that achieve varying levels of success, as well as new objective functions that involve
149 regularizing the mutual information between the high-dimensional data and latent distribution (e.g.,
150 Zhao et al. 2017; Rezaabad and Vishwanath 2019; reviewed by Poole et al. 2019).

151 For VAE-SNE, we provide an effective solution to this problem with the addition of a stochastic
152 neighbor regularizer (Appendix B; van der Maaten and Hinton 2008; van der Maaten 2009; Chien and Hsu
153 2017; Ding et al. 2018) that optimizes pairwise similarity kernels between the high- and low-dimensional
154 distributions to strengthen local neighborhood preservation and more explicitly retain a useful
155 representation. We also draw on other theoretical and practical improvements from the literature to
156 enhance the performance of VAE-SNE (Methods). For example, we use a Gaussian mixture prior for
157 learning the latent distribution (Kingma et al., 2014; Dilokthanakul et al., 2016; Tomczak and Welling,
158 2017). This choice of distribution allows for better local structure preservation and, when combined with
159 sparse watershed assignment to merge overlapping mixture components (Fig. 1; Methods; Todd et al.
160 2017), serves as a flexible method for clustering data – without the need to manually define the number
161 of clusters or impose strong assumptions about cluster shape. We employ several other advances to
162 further improve structure preservation. For instance, we apply a perplexity annealing technique (Kobak
163 and Berens, 2019) to slowly decay the size of the local neighborhoods optimized by the model during
164 training, which helps to preserve structure across multiple scales. Moreover, we extensively optimize the
165 algorithms underlying our model by applying parallel computations on the CPU and GPU that
166 dramatically improve processing speed compared to previous work (Ding et al., 2018).

167 In addition to our three main contributions, we further extend VAE-SNE to demonstrate its flexibility
168 as a framework for dimensionality reduction. To accomplish this, we introduce a von Mises-Fisher
169 variant of VAE-SNE (Appendix C.1; Fig. S10; Video S8, Video S9) that embeds data in polar coordinates
170 (rather than Euclidean coordinates) on a 3-D unit sphere, which is potentially a more natural
171 representation for many high-dimensional datasets (Davidson et al., 2018) and solves the “crowding”
172 problem common to some methods (van der Maaten and Hinton, 2008; Ding and Regev, 2019). Finally,
173 we also apply a modified convolutional version of VAE-SNE (Appendix C.2; Figs. S11, S12) to visualize
174 natural history images of animal specimen collections (Cuthill et al., 2019; Zhang et al., 2019) by directly
175 embedding the raw pixel data. Our results for these two extensions are described in Appendix C.

176 **2.1 Comparisons with other dimension reduction algorithms**

177 Current methods for dimensionality reduction generally fall into two classes known as *linear* and
178 *nonlinear* algorithms. Linear algorithms, such as principal components analysis (PCA), compress
179 high-dimensional data by learning linearly weighted combinations (affine transformations) of the
180 original feature set. Typically these algorithms are optimized to preserve the global structure of the data,
181 where local neighborhood relationships are distorted in order to maintain the full coordinate system of
182 the original features as best as possible. On the other hand, nonlinear algorithms (sometimes called
183 manifold learning algorithms) such as t-SNE (van der Maaten and Hinton 2008) and uniform manifold
184 approximation and projection (UMAP; McInnes et al. 2018) typically take the opposite approach of

185 prioritizing relative relationships between data points rather than the global coordinate system. This
186 approach allows local neighborhoods to be preserved while potentially sacrificing information about the
187 larger-scale relationships between data points in the global coordinate space — although, as we
188 demonstrate here, the global distortion imposed by many of these algorithms is actually comparable to
189 that of PCA.

190 To validate VAE-SNE as a general-purpose method for dimensionality reduction, we quantitatively
191 compare its performance with other dimension reduction algorithms — both linear and nonlinear — using
192 two datasets from different domains (see Methods) describing animal body part dynamics (Berman
193 et al., 2014, 2016; Pereira et al., 2019) and single-cell RNA-seq expression profiles for hippocampal
194 neurons (La Manno et al., 2018). We benchmark multiple variants of VAE-SNE with different pairwise
195 similarity kernels for preserving local neighborhood information (including kernel functions with learned
196 parameters; Appendix B), and we compare these results with those from two high-performance variants
197 of t-SNE (van der Maaten and Hinton, 2008) known as Flt-SNE (Linderman et al., 2017, 2019) and
198 Barnes-Hut-SNE (van der Maaten, 2014), as well as UMAP (McInnes et al., 2018), and two other deep
199 neural network-based dimension reduction methods: scvis (Ding et al., 2018), and ivis (Szubert et al.,
200 2019). We also apply PCA in 2, 5, 10, and 100 dimensions for a linear baseline comparison. We fit each
201 algorithm with a training set and also embed an out-of-sample test set to assess generalization to new
202 data. For both the training and test sets, we then quantitatively assess each algorithm's ability to
203 preserve different types of information about the high-dimensional data when compressing the data to
204 two dimensions, including local, global, fine-scale, and temporal information (Methods). We quantify
205 local information preservation for each algorithm by measuring the preservation of both metric
206 (distance- or radius-based) and topological (nearest neighbors-based) neighborhoods that are
207 approximately 1% of the total embedding size; we measure global information preservation by
208 calculating the correlation between pairwise distances in high- and low-dimensional space; we assess
209 fine-scale information by measuring neighborhood preservation for multiple neighborhood sizes $< 1\%$
210 of the total embedding size; and we evaluate temporal information preservation by computing the
211 correlation between high- and low-dimensional temporal derivatives in a timeseries dataset. Overall the
212 qualitative properties of the embeddings produced by each algorithm are strikingly similar within
213 datasets (Fig. 2), which likely indicates shared mathematical properties of how the latent distributions
214 are modelled. However, we do find potentially important quantitative differences between these
215 algorithms in terms of information preservation and processing speed. We summarize our overall
216 assessments of each nonlinear dimension reduction algorithm in Tables S1, S2, S3.

217 **2.1.1 Local structure preservation**

218 We find that VAE-SNE compares closely to Flt-SNE (Linderman et al., 2017), Barnes-Hut-SNE (van der
219 Maaten, 2014), and UMAP (McInnes et al., 2018) in preserving local structure for both the training set
220 (Figs. S1a, S2a, S5a) and test set (Figs. S3a, S4a), while scvis (Ding et al., 2018) and ivis (Szubert et al.,
221 2019) perform slightly worse. Our results show that VAE-SNE with a t-SNE similarity kernel (van der
222 Maaten and Hinton, 2008) performs the best for preserving local structure, but VAE-SNE with a Gaussian
223 SNE kernel (Hinton and Roweis, 2003) also performs well — similarly to scvis (Ding et al., 2018) and ivis
224 (Szubert et al., 2019). We also find that learning the similarity kernel parameters (for both Gaussian and
225 Student's t kernels) as a function of each data point does not improve performance for our local
226 preservation metrics. The top performing algorithms for local structure preservation (VAE-SNE, t-SNE,
227 and UMAP) are closely comparable to 5-dimensional PCA for both metrics we used to assess local
228 neighborhood preservation.

229 **2.1.2 Global structure preservation**

230 We find that VAE-SNE also does well in preserving global structure for both the training set (Figs. S1a,
231 S2b, S5a) and test set (Figs. S3a, S4b). VAE-SNE with a Gaussian SNE kernel performs best for this
232 metric, but VAE-SNE with a t-SNE kernel also performs nearly as well. Notably all the

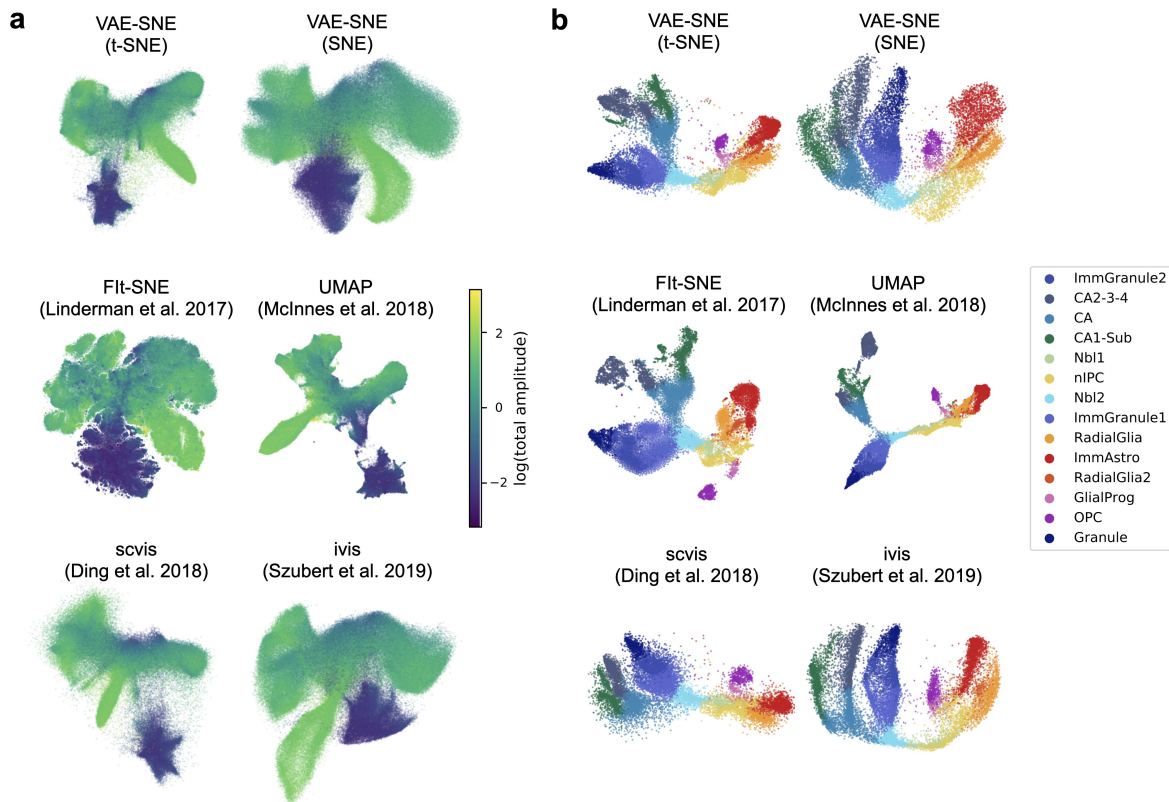


Figure 2. Embeddings for body posture dynamics and single-cell RNA-seq data. **a**, 2-D embeddings of body posture dynamics data from Berman et al. (2014, 2016); Pereira et al. (2019) for each algorithm we tested. The color of each point indicates the logarithm of the total amplitude (overall movement) of body parts for each observation. **b**, 2-D embeddings of single-cell RNA-seq data of developing hippocampal neurons from La Manno et al. (2018) for each algorithm. The color of each point indicates the cell type for that observation as described by La Manno et al. (2018).

233 neural-network-based methods (VAE-SNE, scvis Ding et al. 2018, ivis Szubert et al. 2019) outperform
234 both t-SNE and UMAP (McInnes et al., 2018) in preserving global structure for both datasets we tested.
235 This is perhaps not surprising given that recent work has shown neural network models tend to learn the
236 same axes as PCA (Rolinek et al., 2019). Additionally, these results show that learning the similarity
237 kernel parameters as a function of each data point does improve global structure preservation for
238 VAE-SNE with a t-SNE kernel – likely because it is optimized to be more similar to the Gaussian kernel
239 used to calculate high-dimensional similarities (Appendix B). The top performing algorithms for this
240 metric are comparable to 2-dimensional PCA, which demonstrates that nonlinear algorithms are capable
241 of preserving the same global information as PCA while also better preserving local structure. On one
242 hand, The scvis (Ding et al., 2018) algorithm in particular excels at preserving global structure for the
243 single-cell RNA-seq dataset we tested (Fig. S5a). On the other hand, ivis (Szubert et al., 2019) performs
244 much more poorly than the other neural network algorithms for this dataset, and Fit-SNE (Linderman
245 et al., 2017, 2019) and Barnes-Hut-SNE (van der Maaten, 2014) perform even worse. We also show that
246 UMAP (McInnes et al., 2018) with PCA initialization better preserves global structure than the default
247 Laplacian Eigenmap initialization.

248 **2.1.3 Fine-scale structure preservation**

249 In addition to local and global structure preservation, we evaluate the ability of each algorithm to
250 preserve very fine-scale neighborhood information (Figs. S1b, S3b, S5b). We find that both Fit-SNE
251 (Linderman et al., 2017) and Barnes-Hut-SNE (van der Maaten, 2014) excel at preserving this fine-scale
252 information for the posture dynamics dataset (Figs. S1b, S3b) while every other nonlinear algorithm
253 performs relatively poorly for both the training and test set. For the single-cell RNA-seq dataset, this
254 distinction is not nearly as large and the algorithms all perform more similarly (Fig. S5b), which indicates
255 performance varies depending on the dataset. Performance for the ivis algorithm (Szubert et al., 2019)
256 is especially poor for this metric on the single cell RNA-seq dataset. However, neighborhood
257 membership for neighborhoods between 1% and 10% of the total embedding size are all similarly
258 well-preserved for each algorithm.

259 **2.1.4 Temporal structure preservation**

260 Because one of the datasets we use for benchmarking is a behavioral timeseries, for these data we also
261 assess the temporal structure preservation of each algorithm (Figs. S3a, S4c) on the out-of-sample test
262 set (the training set is randomly sampled across multiple timeseries, so temporal information is not
263 preserved). We find that VAE-SNE (particularly the SNE kernel variant), Fit-SNE (Linderman et al., 2017),
264 Barnes-Hut-SNE (van der Maaten, 2014), scvis (Ding et al., 2018), and ivis (Szubert et al., 2019) perform at
265 the same level as 5-dimensional PCA in preserving temporal structure, while UMAP (McInnes et al., 2018)
266 performs relatively poorly in comparison to the other algorithms – even worse than 2-dimensional PCA.

267 **2.1.5 Speed comparisons**

268 In addition to assessing information preservation, we also compare the speed of each algorithm
269 both when fitting the algorithm to the training set (Figs. S1c, S5c) and when embedding an out-of-sample
270 test set (Figs. S3c, S5c). We find that training time increases approximately linearly with the size of the
271 dataset for each algorithm. UMAP (McInnes et al., 2018) has the fastest training time (approximately as
272 fast as PCA), followed by Fit-SNE (Linderman et al., 2017) and Barnes-Hut-SNE (van der Maaten, 2014),
273 and then VAE-SNE. While VAE-SNE is slower for fitting the training set than both UMAP (McInnes et al.,
274 2018) and t-SNE, it is much faster than the other two neural network methods scvis (Ding et al., 2018)
275 and ivis (Szubert et al., 2019). We also demonstrate that VAE-SNE, and the other neural network
276 methods, can quickly embed out-of-sample test data (Figs. S3c, S5c). The time needed for embedding
277 new data is much higher for both t-SNE and UMAP, and while the elapsed time for embedding the test
278 set scales linearly with the number of samples for all algorithms, we also find that it increases with the

279 size of the training set for both UMAP (McInnes et al., 2018) and Barnes-Hut-SNE (van der Maaten, 2014)
280 (Fig. S3c). This is almost certainly because adding new data for these algorithms requires calculating
281 approximate nearest neighbors between the out-of-sample data and the training set, which consequently
282 requires more computation time for larger training sets. Unexpectedly, Fit-SNE (Linderman et al., 2017)
283 does not exhibit this behavior despite using similar nearest neighbor calculations to Barnes-Hut-SNE
284 (van der Maaten, 2014). On the other hand, VAE-SNE and other deep learning algorithms do not suffer
285 from this limitation. Finally, while we do not comprehensively assess memory complexity of different
286 algorithms in this paper, we stopped our speed comparisons at data subsets with 232,000 ($\times 1500$
287 dimensions) observations because UMAP began to cause out-of-memory errors for larger subsets –
288 while all of the other algorithms we tested could still successfully run under the same conditions. This
289 helps to illustrate the key advantage of deep learning-based methods, which naturally maintain very low
290 memory complexity by applying optimization using small batches of data.

291 **2.2 Using the likelihood to assess out-of-sample data**

292 Because VAE-SNE also calculates a likelihood score for reconstructing the original high-dimensional
293 data, we can use this to assess performance on out-of-sample data, which is an idea originally proposed
294 by Ding et al. (2018). To test this, we calculate the likelihood score for real data from the posture
295 dynamics dataset (Berman et al., 2014, 2016; Pereira et al., 2019) and randomly-permuted data
296 (randomized across feature columns) from the same dataset. We find that the likelihood score is reliably
297 lower for the randomized data, and the two likelihood distributions are well separated (Fig. S6a), which
298 shows this metric could potentially be used to detect outliers. We also compare the entropy of the
299 approximate posterior distribution for each embedded sample as another potential metric for detecting
300 outliers. While we find that the entropy is much higher for the randomized data, the distribution is highly
301 overlapping with the entropy for the real data (Fig. S6b), which indicates the entropy may not be as
302 useful for evaluating the embedding quality.

303 **2.3 Clustering body posture dynamics to reveal stereotyped behavioral organization**

304
305 To demonstrate its capabilities as a clustering algorithm, we use VAE-SNE to automatically discretize a
306 dynamical time series dataset describing the high-dimensional body posture and behavioral repertoire of
307 59 freely-behaving fruit flies (*D. melanogaster*; Berman et al. 2014, 2016; Pereira et al. 2019) – a
308 commonly-used model organism for neuroscience, pharmaceutical, and genetics research. To
309 accomplish this, we use the annotated training data from (Pereira et al., 2019) to train a pose estimation
310 model using deep learning-based software (DeepPoseKit; Graving et al. 2019). We then use this trained
311 model to automatically track the spatial locations of 10 body parts (head, legs, wings, abdomen) directly
312 from video timeseries data and generate time-frequency spectrograms describing body-part dynamics
313 for each observation in the timeseries (Berman et al., 2014), which naturally incorporates multi-scale
314 temporal information into each data vector. We then apply VAE-SNE to compress the data to a
315 30-dimensional latent embedding and simultaneously discretize the dynamical posture timeseries into a
316 set of behavioral clusters. We find that, after optimizing the 30-D VAE-SNE model for 5 repeated trials
317 using the full 21.1 million observation dataset and applying sparse watershed assignment to generate
318 cluster labels (Methods; Fig. 1d; Todd et al. 2017), VAE-SNE consistently learns a total of 26 low-level
319 behavioral clusters describing distinct, stereotyped body part movements. We also achieve similar
320 (nearly identical) results when clustering in 10-D and 50-D space and when varying the number of
321 components in the Gaussian mixture prior used for clustering – provided that the number of
322 components is large enough (e.g., $K \geq 100$).

323 To provide a broad overview of the behavioral structure discovered by VAE-SNE, we manually group
324 these low-level clusters into 6 high-level clusters (Figs. 3, S7; Video S1) by examining video clips
325 sampled from each cluster (Video S2–Video S7) and by calculating and visualizing the mean
326 spectrograms for each low-level cluster to quantify the average distribution of body part movements

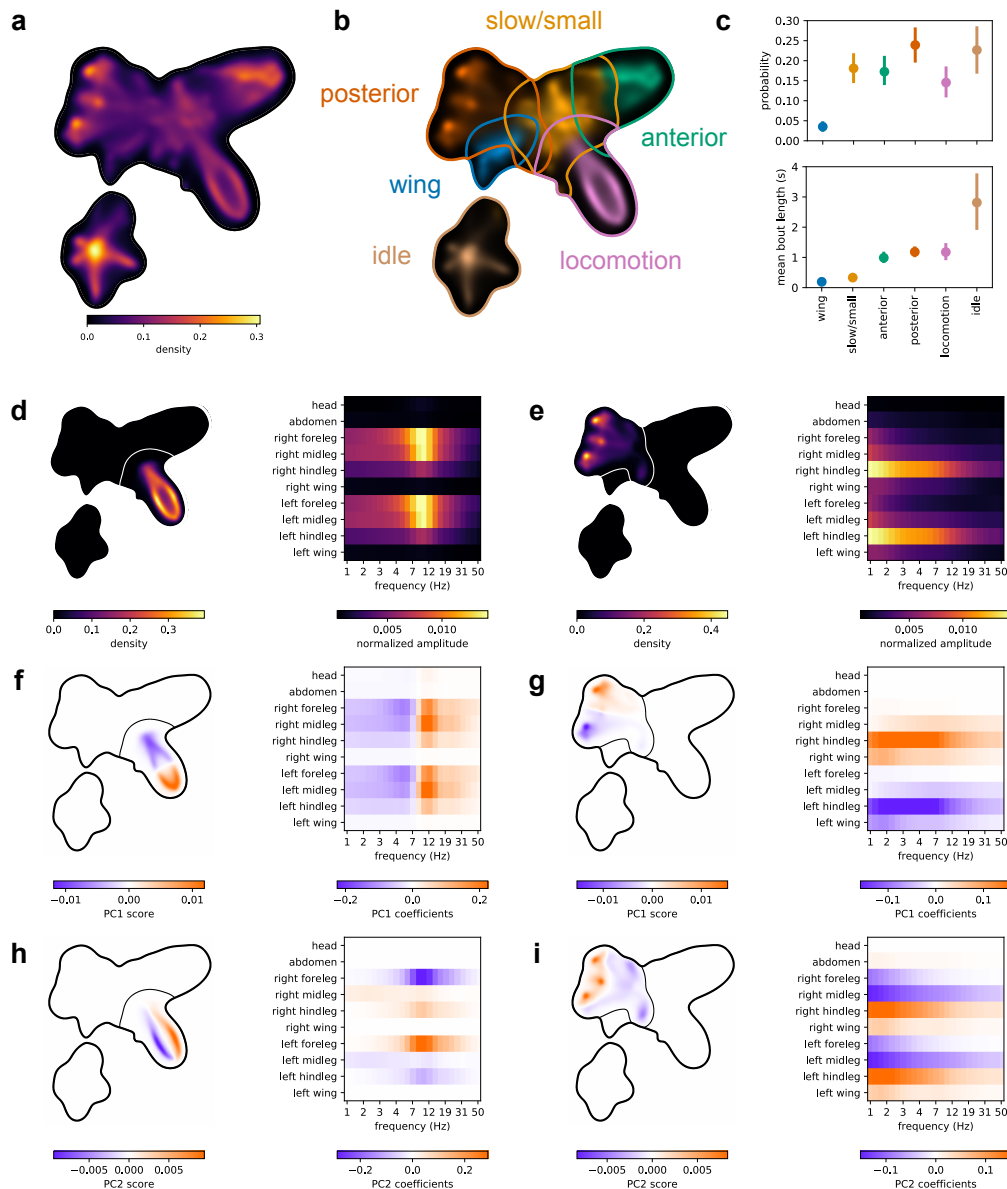


Figure 3. Clustering body posture dynamics. **a**, The posterior probability density for the full 21.1 million observation body posture dynamics dataset from Berman et al. (2014, 2016); Pereira et al. (2019) embedded using a 2-dimensional VAE-SNE model. **b**, The manually-grouped high-level cluster assignments produced using the learned prior from a 30-dimensional VAE-SNE embedding visualized in the 2-D embedding, where contours are the largest 90% probability density contour for each cluster distribution. **c**, Mean and 95% bootstrap intervals of the marginal (stationary) probability and mean bout length for each high-level cluster ($n = 59$ per cluster). **d-i**, Visualizations describing the high-level locomotion (**d,f,h**; Video S2; Fig. S8) and posterior grooming (**e,g,i**; Video S4; Fig. S9) clusters. **d-e**, The 2-D posterior probability density for each cluster (left) and the mean spectrogram for each cluster (right). **f-i**, The principal component scores for the two largest components of the spectrograms assigned to each cluster visualized within the 2-D embedding (left), and the eigenvector coefficients describing the linear contribution of each spectrogram feature (right) for the principal component score.

327 across frequencies for each behavioral class (Figs. S8d-f, S9d-i). These high-level clusters include:
328 locomotion (Video S2), anterior grooming (Video S3), posterior grooming (Video S4), wing movements
329 (Video S5), small/slow leg movements (Video S6), and idle behavior (Video S7). Many of the low-level
330 clusters (10 clusters in total) describe distinct slow/small leg movements, while there are 3 low-level
331 clusters for locomotion (Fig. S8), 3 for anterior grooming, 6 for posterior grooming (Fig. S9), 2 for wing
332 movements, and 2 for idle behavior. Videos and posture timeseries data sampled from each cluster also
333 clearly demonstrate the stereotypy of behaviors within these behavioral classes, which matches well
334 with previous work describing these dynamics (Berman et al., 2014, 2016; Klibaite et al., 2017; Klibaite
335 and Shaevitz, 2019; Pereira et al., 2019). Additionally, the principal components of the spectrograms
336 from each high-level cluster (Fig. 3f-i; Fig. S7d-i) reveal continuous variation related to asymmetrical
337 body movements and differences in peak movement frequency. We calculate basic statistics describing
338 cluster usage across individuals (Figs. 3c, S8c, S9c) including the marginal (stationary) probability of
339 behavioral classes across individuals and the mean bout length, or the average amount of time a
340 behavior is performed when an individual transitions into that cluster. In particular, the low probability
341 and short bout length for wing movements and short bout length for slow/small leg movements (Fig. 3c)
342 indicate these clusters may be transitional or idiosyncratic behaviors (Todd et al., 2017). For the low-level
343 locomotion clusters (Fig. S8) we also calculate the forward component of the leg movement velocity (in
344 body lengths per second, or $BL \cdot s^{-1}$) relative to the egocentric orientation of the animal. We then use
345 the forward velocity to classify each leg in the timeseries as “swing” (forward velocity $> 0 BL \cdot s^{-1}$) or
346 “stance” (forward velocity $\leq 0 BL \cdot s^{-1}$) and find that our low-level locomotion clusters show signatures
347 of distinct locomotory gaits (i.e., tetrapod and tripod gaits; Mendes et al. 2013; Pereira et al. 2019) with
348 different numbers of legs being used for walking, on average, within each cluster. Together these results
349 demonstrate that VAE-SNE is able to automatically decompose the dynamics of known complex
350 behaviors (Video S1).

351 Due to the many philosophical complexities of objectively evaluating unsupervised cluster
352 representations (reviewed by Jain et al. 1999; Kleinberg 2003; Todd et al. 2017), we forgo any further
353 quantitative assessment of our clustering results and instead leave this for future work. For example, it
354 is unclear how to best select the number of clusters for many different algorithms; how to properly
355 compare algorithms that naturally produce different numbers of clusters and cluster shapes; and what
356 metric(s) should be used to meaningfully evaluate a clustering description as generally “good” or
357 “useful” other than manual, qualitative validation of the results, which we already provide here – though
358 several quantitative descriptors with varying levels of desirability have been recently proposed for
359 behavioral data (Todd et al., 2017). Comparing unsupervised cluster labels with a priori-defined labels –
360 as is common practice (e.g., Jiang et al. 2016; Xie et al. 2016; Guo et al. 2017; Yang et al. 2019; Luxem
361 et al. 2020) – is also problematic, as human-supervised descriptions may not accurately capture the
362 underlying structure of the data distribution, and this is especially true for datasets where the goal is to
363 potentially discover subtle differences that are undetectable by humans (e.g., Wiltshko et al. 2015).
364 Despite the limitations imposed by these complexities, our results still illustrate multiple useful features
365 of VAE-SNE as a general-purpose method.

366 Overall, we demonstrate how VAE-SNE can be used as a practical, scalable, and flexible tool for
367 clustering real-world high-dimensional data. In this case, we transform posture data into interpretable
368 behavioral labels that are comparable to those from previous methods (Berman et al., 2014, 2016; Todd
369 et al., 2017; Klibaite et al., 2017; Cande et al., 2018; Klibaite and Shaevitz, 2019; Pereira et al., 2019).
370 However, in contrast to many of these existing methods, VAE-SNE performs dimension reduction and
371 clustering simultaneously, and unlike most previously-described algorithms for clustering data (e.g.,
372 Jiang et al. 2016; Xie et al. 2016; Guo et al. 2017; Yang et al. 2019), our method learns a small set of
373 decipherable classes without the need to carefully tune the number of clusters fitted to the data, which
374 can often be a non-trivial, unintuitive, and computationally-intensive process (Milligan and Cooper, 1985;
375 Pham et al., 2005; Fang and Wang, 2012; Todd et al., 2017). Instead, any arbitrarily large number will give
376 similar results due to the sparse watershed assignment procedure we use to combine overlapping
377 clusters (Methods; Fig. 1d; Todd et al. 2017). In contrast to methods that impose strong assumptions
378 about cluster shape, our clustering method has relaxed assumptions and allows for arbitrarily complex

379 (e.g., non-convex) cluster distributions based on the local structure of the data. Additionally, in
380 comparison to prior methods for unsupervised behavioral analysis, VAE-SNE has the advantage of being
381 able to use more than two dimensions for clustering data, which has been shown to provide
382 higher-quality behavioral labels with many potentially-desirable properties (Todd et al., 2017). Finally, our
383 results further show that there is no need to carefully select a subset of data to use for training (e.g., the
384 importance sampling technique described by Berman et al. 2014), which can also be a time-consuming
385 process. Instead, VAE-SNE can be readily applied to large datasets that cannot fit into memory while still
386 successfully detecting relatively short-lived and infrequent types of behavior, such as wing movements
387 (Fig. 3b-c; Video S5).

388 **3 Discussion**

389 Here we introduce VAE-SNE, a deep generative model for simultaneously reducing dimensionality and
390 clustering data. We compare VAE-SNE to existing methods for dimensionality reduction and
391 demonstrate its utility and versatility using real-world examples. Our results establish that VAE-SNE is
392 able to generate robust and interpretable compressed representations for data from different domains
393 and is comparable in performance to other nonlinear methods for dimensionality reduction. In contrast
394 to these existing methods, VAE-SNE has the advantage of being able to automatically cluster similar
395 observations into a small set of classes, which can then be used to summarize large datasets with a
396 coarse-grained description or select specific subpopulations of data for more detailed analysis. Our
397 approach can also readily scale to very large datasets by leveraging techniques from deep learning –
398 including, and especially, out-of-core data that cannot fit into memory. However, despite these strengths,
399 VAE-SNE still has important limitations depending on the goals of the user, and there are many ways in
400 which the model could be improved or extended in subsequent iterations. There are also other domains
401 that VAE-SNE could be applied to in the future.

402 VAE-SNE preserves local relationships while also minimizing global structure distortion. Additionally,
403 while VAE-SNE is not explicitly an autoregressive model, it still preserves a good deal of
404 high-dimensional timeseries information. However, our results also show that VAE-SNE, and most of the
405 other dimension reduction methods we tested, does not accurately preserve fine-scale structure
406 (neighborhoods <1% of the total embedding size). For many applications, preserving these details may
407 be unimportant, but this structure has been shown to be useful for detecting infrequent types of data,
408 such as rare cell types (Linderman et al., 2019). Therefore, our results suggest that if researchers wish to
409 preserve this type of information they should use Fit-SNE (Linderman et al., 2017, 2019) or
410 Barnes-Hut-SNE (van der Maaten, 2014) over other algorithms for dimension reduction. We also find that,
411 when initialized with PCA over the default initialization, UMAP (McInnes et al., 2018) preserves global
412 structure slightly better without noticeably affecting local structure preservation, so PCA may be a more
413 advantageous choice for initializing UMAP embeddings.

414 VAE-SNE optimizes faster than existing deep learning methods for dimensionality reduction, but
415 Fit-SNE (Linderman et al., 2017, 2019), Barnes-Hut-SNE (van der Maaten, 2014), and UMAP (McInnes
416 et al., 2018) are still faster. However, the training time for deep-neural-network methods like VAE-SNE
417 and *ivis* (Szubert et al., 2019) can be variable due to the use of early stopping criteria that automatically
418 end training when no improvement in the objective function is detected. These early stopping criteria
419 could be easily adjusted to further shorten (or lengthen) training time. While we did not assess
420 performance during the optimization process, much of the training time for VAE-SNE is spent on minor
421 improvements to the objective function, which indicates adequate results can also be achieved with less
422 training time. Additionally, Fit-SNE (Linderman et al., 2017, 2019), Barnes-Hut-SNE (van der Maaten,
423 2014), and UMAP (McInnes et al., 2018), are much slower for embedding new data because they
424 calculate nearest neighbors for the new data and further optimize the embedding, which VAE-SNE does
425 not require due to its learned encoder function. For smaller datasets that can fit in memory Fit-SNE
426 (Linderman et al., 2017, 2019), Barnes-Hut-SNE (van der Maaten, 2014), and UMAP (McInnes et al., 2018)
427 are still attractive options for dimensionality reduction, but for datasets that do not fit into memory,

428 VAE-SNE provides some distinct advantages.

429 VAE-SNE has the ability to detect outliers and assess the embedding quality for out-of-sample data.
430 This provides a straightforward mechanism for identifying new data to include in the training set, which
431 can further improve performance. Most of the other algorithms we tested, or at least the specific
432 software implementations we tested, provide no mechanism for quantitatively assessing embedding
433 quality for each observation – with outliers being simply embedded under the assumption that the data
434 are well supported by the training distribution. This can cause problems for any downstream analysis,
435 especially when using statistical tests to answer scientific questions. Further improvements for outlier
436 detection might include the use of Bayesian inference (Hafner et al., 2018) or other methods for
437 estimating predictive uncertainty (reviewed by Kendall and Gal 2017).

438 We demonstrate that results produced by VAE-SNE can serve as a highly-interpretable coarse-grained
439 description of tens-of-millions of observations – with several advantages over existing methods for
440 clustering data. Applying VAE-SNE to future research in the behavioral sciences could help to reveal the
441 genetic, environmental, and neural underpinnings of animal behavior (Berman, 2018; Brown and
442 De Bivort, 2018; Datta et al., 2019) – especially when combined with recent advances in behavioral
443 measurement (Mathis et al., 2018; Pereira et al., 2019; Graving et al., 2019; Günel et al., 2019) as well as
444 genetic (Ran et al., 2013; Doudna and Charpentier, 2014), sensory (Stowers et al., 2017), and neural (Bath
445 et al., 2014; Cande et al., 2018) manipulations. The clustering capabilities of VAE-SNE could also be
446 applied to other types of data, such as single-cell RNA-seq data (Ding et al., 2018; La Manno et al., 2018)
447 and natural history images (Cuthill et al., 2019; Zhang et al., 2019), but we leave this as future work for
448 other researchers and domain experts to explore and validate. VAE-SNE might also be further improved
449 by the use of more complex hierarchical clustering distributions (Tomczak and Welling, 2017; Roberts
450 et al., 2018; Razavi et al., 2019), where additional scales with finer- or coarser-grained descriptions can
451 be selected from the model for post-hoc analysis. Recent work has also shown that iteratively adjusting
452 the parameters of the t-SNE similarity kernel can be used to generate a hierarchy of clusters in the latent
453 embedding (Robinson and Pierce-Hoffman, 2020), which could be potentially applied to VAE-SNE as well.

454 To demonstrate the flexibility of VAE-SNE as a deep learning model, we introduce a variant for
455 embedding data in polar coordinates on a unit sphere (Appendix C.1). We find that VAE-SNE successfully
456 preserves structure in a spherical embedding as well (Fig. S10; Video S8; Video S9), which may be a
457 more natural way to model some high-dimensional data sets (Davidson et al., 2018) since it avoids the
458 “crowding” problem common to other embedding methods (van der Maaten and Hinton, 2008; Ding and
459 Regev, 2019). While we focus on the Euclidean and cosine distances for calculating local neighborhoods,
460 any differentiable distance function could potentially be substituted to create different embedding
461 geometries, and, while we focus on kernels from the location-scale family of probability distributions (i.e.
462 Gaussian, Student’s t), other log probability functions could potentially be used as well.

463 We also introduce a convolutional version of VAE-SNE for embedding images directly from raw pixel
464 data (Appendix C.2). After applying this model to natural history images, we find that it groups
465 perceptually-similar images based on complex sets of image features that correspond with taxonomic
466 groupings (Figs. S11, S12). These results indicate that convolutional VAE-SNE may be useful for tasks
467 such as relating distributions of complex animal coloration patterns to ecological, evolutionary, and
468 behavioral function (Cuthill et al., 2017, 2019; Ezray et al., 2019; Wham et al., 2019). Future applications
469 might include applying VAE-SNE to audio data (e.g., Oord et al. 2016; Sainburg et al. 2019).

470 There are multitude of ways in which VAE-SNE could be further improved or extended. Naturally,
471 future work could apply more recent advances in variational and probabilistic inference like normalizing
472 flows (Rezende and Mohamed, 2015; Kingma et al., 2016; Papamakarios et al., 2017), which allow data to
473 be modeled with a more direct invertible mapping from the latent posterior to the data distribution, while
474 also employing flexible, arbitrarily-complex distributions. The latent distribution used for VAE-SNE could
475 also be modeled using many other types of representations such as quantized (Van Den Oord et al.,
476 2017) or categorical (Jang et al., 2016; Maddison et al., 2016) distributions. Recent progress in
477 generative adversarial networks (GANs; Goodfellow et al. 2014), may also provide further enhancements
478 for modeling complex feature dependencies within the data distribution (Larsen et al., 2016; Srivastava
479 et al., 2017; Dieng et al., 2019b). Timeseries data could be explicitly modeled using autoregressive deep

480 neural networks (e.g., Oord et al. 2016) for the encoder and decoder similar to Wiltchko et al. (2015);
481 Johnson et al. (2016b); Sussillo et al. (2016); Markowitz et al. (2018); Pandarinath et al. (2018); Luxem
482 et al. (2020), and the latent distribution can be optimized to accurately predict future observations,
483 which has been shown to be a useful framework for modeling behavior (Berman et al., 2016; Luxem et al.,
484 2020). Additionally, computational efficiency might be further improved by applying recent advances in
485 metric (Sohn, 2016) and contrastive learning (Chen et al., 2020), which may reduce or eliminate the need
486 to perform expensive pairwise computations. Recent work on density-preserving versions of t-SNE and
487 UMAP (Narayan et al., 2020) could also be incorporated to further improve the embedding quality.

488 Explicitly modeling hierarchical structure caused by variance across individual trials and subjects
489 (Pandarinath et al., 2018) and batch effects due to variance in sampling procedures (Ding and Regev,
490 2019) is also important for improving VAE-SNE in the future. These effects could be accounted for with
491 more complex, hierarchically-parameterized models (Sussillo et al., 2016; Pandarinath et al., 2018),
492 hierarchical latent distributions (Tomczak and Welling, 2017; Roberts et al., 2018; Razavi et al., 2019), and
493 new similarity kernels – such as the conditional t-SNE kernel recently proposed by Kang et al. (2019).
494 The general use of conditional (e.g., Van den Oord et al. 2016) or supervised (e.g., Alemi et al. 2016)
495 labels when optimizing the model could also help to integrate additional prior information about the data
496 distribution into the latent distribution, the latter of which is already a feature of both UMAP (McInnes
497 et al., 2018) and ivis (Szubert et al., 2019).

498 In summary, VAE-SNE is a general-purpose deep learning model for both dimension reduction and
499 clustering that can be applied to many different types of data and readily scales to large datasets.
500 Together our results illustrate that it is a robust, feature-rich method with multiple distinct advantages
501 that make it an effective tool for analyzing real-world datasets across disciplines.

502 **4 Methods**

503 **4.1 The VAE-SNE model**

504 VAE-SNE is a variational autoencoder (VAE; Appendix A.1) with a learned Gaussian mixture prior (Kingma
505 et al., 2014; Dilokthanakul et al., 2016; Tomczak and Welling, 2017) that is optimized using the ELBO
506 objective function (derived in Appendix A.2) with an additional local neighborhood regularizer (Hinton
507 and Roweis, 2003; van der Maaten and Hinton, 2008; van der Maaten, 2009; Ding et al., 2018). The
508 likelihood and divergence terms from the ELBO objective can be broadly considered as an information
509 theoretic trade-off between reconstruction accuracy (distortion) and compression (rate) respectively
510 (Alemi et al., 2016; Chalk et al., 2016; Alemi et al., 2017), which makes VAEs an attractive solution for
511 dimensionality reduction. However, there are implicit problems with the ELBO objective (reviewed by
512 Alemi et al. 2017; Dieng et al. 2019a) that may prevent the model from learning a useful latent
513 representation – e.g., a powerful, overparameterized decoder can simply ignore the compressed latent
514 codes but still produce high-quality reconstructions. These issues render VAEs problematic as a general
515 method for reducing dimensionality, as the primary purpose of dimensionality reduction is to create
516 compressed representations that preserve important statistical features of the original data distribution.

517 **4.1.1 Regularizing the ELBO to improve structure preservation**

518 We address the problems outlined above by optimizing VAE-SNE with a regularized version of the ELBO.
519 This modification introduces a pairwise similarity regularizer derived from the (t -distributed) stochastic
520 neighbor embedding (SNE/t-SNE) objective (Hinton and Roweis, 2003; van der Maaten and Hinton, 2008;
521 van der Maaten, 2009). This idea of using the SNE objective for regularizing the latent space of VAEs
522 was first proposed by Chien and Hsu (2017), which they called variational manifold probabilistic linear
523 discriminant analysis (vm-PLDA), and later independently proposed by Ding et al. (2018) with their scvis
524 model. However, the idea of applying the SNE objective to autoencoders, and deep neural networks in
525 general, was introduced much earlier by van der Maaten (2009) with parametric t-SNE (pt-SNE), who

526 proposed to use this objective in conjunction with an autoencoder to jointly learn a latent embedding.
 527 The pt-SNE model (van der Maaten, 2009) was also recently combined with advances from the
 528 Barnes-Hut-SNE algorithm (van der Maaten, 2014) under the name net-SNE (Cho et al., 2018).
 529 Additionally, Moody (2017) developed one of the first publicly-available pieces of software to combine
 530 the SNE objective with variational inference (variational t-SNE, or vt-SNE; and topic-SNE) but did not use
 531 a deep neural network to amortize inference across a set of shared parameters. Im et al. (2018) also
 532 proposed a variational bound on the t-SNE objective to improve optimization.

533 Here we apply the SNE objective to a VAE in a similar fashion to Ding et al. (2018). That is, we use the
 534 SNE objective as a method of better preserving structure in the latent embedding produced by our VAE,
 535 which improves the usefulness of the compressed representation (approximate posterior) produced by
 536 the ELBO. When combined into a single objective, we call this the stochastic neighbor evidence lower
 537 bound, or SNEELBO. Generalizing from Ding et al. (2018), given a high-dimensional data matrix
 538 $\mathbf{X} = \{\mathbf{x}_1, \dots, \mathbf{x}_N\}$ and model parameters $\{\theta, \phi\}$, the SNEELBO objective is written as:

$$\arg \min_{\theta, \phi} -\text{SNEELBO}(\mathbf{X}, \theta, \phi) = \arg \min_{\theta, \phi} -\frac{1}{N} \sum_i \text{ELBO}_i(\mathbf{x}_i, \theta, \phi) - \alpha \text{SNE}_i(\mathbf{X}, \phi) \quad (1a)$$

$$\text{ELBO}_i(\mathbf{x}_i, \theta, \phi) = \gamma \underbrace{\mathbb{E}_{\mathbf{z}_i \sim q_\phi(\mathbf{z}|\mathbf{x}_i)} [\log p_\theta(\mathbf{x}_i|\mathbf{z}_i)]}_{\text{distortion}} - \beta \underbrace{\mathbb{KL}[q_\phi(\mathbf{z}|\mathbf{x}_i)||p_\theta(\mathbf{z})]}_{\text{rate}} \quad (1b)$$

$$\text{SNE}_i(\mathbf{X}, \phi) = \mathbb{E}_{\substack{\mathbf{z}_i \sim q_\phi(\mathbf{z}|\mathbf{x}_i) \\ \mathbf{z}_j \sim q_\phi(\mathbf{z}|\mathbf{x}_j)}} \left[\sum_j \text{SNE}_{j|i}(\mathbf{x}_i, \mathbf{x}_j, \phi) \right] \quad (1c)$$

$$= \mathbb{E}_{\substack{\mathbf{z}_i \sim q_\phi(\mathbf{z}|\mathbf{x}_i) \\ \mathbf{z}_j \sim q_\phi(\mathbf{z}|\mathbf{x}_j)}} \left[\underbrace{\sum_j \mathbb{KL}[p(\mathbf{x}_j|\mathbf{x}_i)||q_\phi(\mathbf{z}_j|\mathbf{z}_i)]}_{\text{pairwise similarity}} \right] \quad (1d)$$

539 for $i, j = 1, \dots, N$ and $i \neq j$, where N is the number of observations in the $N \times M$ matrix $\mathbf{X} \in \mathbb{R}^M$. Thus
 540 vectors \mathbf{x}_i and \mathbf{x}_j are the i th and j th row in \mathbf{X} , while \mathbf{z}_i and \mathbf{z}_j are Monte Carlo samples from the
 541 approximate low-dimensional posterior $\mathbf{z}_i \sim q_\phi(\mathbf{z}|\mathbf{x}_i)$ and $\mathbf{z}_j \sim q_\phi(\mathbf{z}|\mathbf{x}_j)$ respectively (Eq. 12c) –
 542 sampled using the reparameterization trick from Kingma and Welling (2013), or $\mathbf{z}_i = \boldsymbol{\mu} + \boldsymbol{\sigma} \odot \boldsymbol{\epsilon}$, where $\boldsymbol{\epsilon}$
 543 is an auxiliary noise variable $\boldsymbol{\epsilon} \sim \mathcal{N}(0, \mathbf{I})$ and \odot is the element-wise product (see Appendix A.3 for further
 544 discussion).

545 The objective function (Eq. 1a) consists of three terms, which can be interpreted as follows: **(1)** the
 546 expected log likelihood of the decoder distribution (Eq. 1b; distortion) minimizes distortion between the
 547 observed ground truth \mathbf{x}_i and reconstruction, or maximizes accuracy, and preserves global structure in
 548 the embedding; **(2)** the divergence between the approximate posterior and the prior distribution (Eq. 1b;
 549 rate) constrains the global coordinate space of the embedding and restricts the rate of information
 550 (relative to the prior) that can be transmitted through the compressed space; and **(3)** the expected
 551 divergence between pairwise similarities (Eq. 1d) in high-dimensional space $p(\mathbf{x}_j|\mathbf{x}_i)$ and those in
 552 low-dimensional space $q_\phi(\mathbf{z}_j|\mathbf{z}_i)$ acts as a regularizer to preserve local neighbor relationships between
 553 data points. Further details of this stochastic neighbor regularizer are derived in Appendix B.

554 The Lagrange multipliers γ, β , and α are used to weight the distortion, rate, and pairwise similarity
 555 terms respectively, which we include as hyperparameters for the model. These multipliers can be
 556 adjusted to produce different forms of the objective for optimizing the model – e.g., increasing or
 557 decreasing the rate with the β multiplier (Higgins et al., 2017) – but in practice we set $\gamma = \beta = 1$, while α
 558 is set (following Ding et al. 2018) to the dimensionality of the data $\alpha = M$ to match the distortion term,
 559 which scales with the size of the input, or $\log p_\theta(\mathbf{x}|\mathbf{z}) = \sum_{m=1}^M \log p_\theta(x_m|\mathbf{z})$.

560 4.1.2 Learning a Gaussian mixture prior

561 For optimizing the VAE-SNE objective (Eq. 1a), we use a learned, or empirical, Gaussian mixture prior for
 562 $p_{\theta}(\mathbf{z})$ which allows for an arbitrarily complex distribution (similar to Kingma et al. 2014; Dilokthanakul
 563 et al. 2016; Tomczak and Welling 2017). Using a more complex distribution allows for a tighter bound on
 564 objective, and, after optimization, approaches the true posterior distribution as the complexity of the
 565 distribution is increased (Kingma et al., 2014; Dilokthanakul et al., 2016; Tomczak and Welling, 2017;
 566 Cremer et al., 2017). The Gaussian mixture distribution is written as the weighted mixture of K Gaussian
 567 components:

$$p_{\theta}(\mathbf{z}) = \sum_{k=1}^K \omega_k \mathcal{N}(\mathbf{z} | \boldsymbol{\mu}_k, \mathbf{I}). \quad (2)$$

568 The mean $\boldsymbol{\mu}_k \in \mathbf{M}$ and mixture weight $\omega_k \in \boldsymbol{\omega}$ of each component are learned as model parameters
 569 $\{\mathbf{M}, \boldsymbol{\omega}\} \in \boldsymbol{\theta}$ subject to a softmax normalization constraint $\sum_{k=1}^K \omega_k = 1$. We also regularize the prior
 570 distribution by minimizing the divergence between the mixture distribution used to weight each
 571 component and a maximum-entropy mixture distribution, or:

$$\arg \min_{\boldsymbol{\omega}} \sum_{k=1}^K \omega_k \log \omega_k + \omega_k \log K. \quad (3)$$

572 This prevents the prior from degenerating to a small number of modes (a problem described in more
 573 detail by Kingma et al. 2014; Dilokthanakul et al. 2016) by increasing the entropy of the mixture
 574 distribution. A higher entropy mixture distribution forces to model to utilize more of the components
 575 within the distribution, which increases the number of clusters and, consequently, the level of detail of
 576 the final clustering description (Still and Bialek, 2004). An analogous maximum entropy regularizer was
 577 also recently applied to solve the long-standing mode collapse problem common to generative
 578 adversarial networks (GANs; Dieng et al. 2019b).

579 The covariance for each component distribution could be learned as free parameters, but we find
 580 that using a simpler identity covariance matrix \mathbf{I} allows for a sufficiently expressive prior distribution
 581 without adding additional complexity – and is less prone to cluster degeneracy during optimization.
 582 Using a highly-flexible (i.e., $K \gg 1$) learned distribution as the prior for the latent space allows for better
 583 structure preservation, as non-convex structures are not distorted by the use of an overly simple prior.
 584 Also note that the special case of $K = 1$ mixture component is equivalent to the standard VAE prior
 585 (Kingma and Welling, 2013), or $p_{\theta}(\mathbf{z}) = \mathcal{N}(\mathbf{z} | 0, \mathbf{I})$, which is the prior used by Ding et al. (2018).

586 **Calculating the rate loss term** The parameters for the Gaussian mixture prior $\{\mathbf{M}, \boldsymbol{\omega}\} \in \boldsymbol{\theta}$ are then
 587 learned from the data via the rate term in the VAE-SNE objective (Eq. 1b). For the special case of $K = 1$
 588 we compute the Kullback-Leibler divergence analytically; however, because there is no analytical solution
 589 for a Gaussian mixture distribution with $K > 1$, we instead approximate this term numerically using
 590 Monte Carlo integration. In this case we use the expected log-density ratio for calculating the rate
 591 (Appendix A.2), which is written as:

$$\mathbb{KL}[q_{\phi}(\mathbf{z} | \mathbf{x}_i) || p_{\theta}(\mathbf{z})] = \int q_{\phi}(\mathbf{z} | \mathbf{x}_i) \log \frac{q_{\phi}(\mathbf{z} | \mathbf{x}_i)}{p_{\theta}(\mathbf{z})} d\mathbf{z} \quad (4a)$$

$$= \mathbb{E}_{\mathbf{z}_i \sim q_{\phi}(\mathbf{z} | \mathbf{x}_i)} \left[\log \frac{q_{\phi}(\mathbf{z}_i | \mathbf{x}_i)}{p_{\theta}(\mathbf{z}_i)} \right] \quad (4b)$$

$$= \mathbb{E}_{\mathbf{z}_i \sim q_{\phi}(\mathbf{z} | \mathbf{x}_i)} [\log q_{\phi}(\mathbf{z}_i | \mathbf{x}_i) - \log p_{\theta}(\mathbf{z}_i)]. \quad (4c)$$

592 **Clustering data with the Gaussian mixture prior** After optimizing the parameters for the prior, we can
593 then use the learned Gaussian mixture to assign embedded data to discrete clusters. In other words, we
594 wish to calculate the conditional distribution $p_{\theta}(\mathbf{y}|\mathbf{z})$, where \mathbf{y} is a vector of class labels, or
595 $\mathbf{y} = \{y_1, y_2, \dots, y_K\}$. However, the Gaussian mixture prior can contain highly-overlapping component
596 distributions, which can cause undesirable side-effects. On one hand, this renders the parameterized
597 mode for each overlapping component an unreliable descriptor of the surrounding local density, as each
598 component is then simply a degenerate sub-mode within a non-Gaussian density cluster rather than a
599 distinct subpopulation within the distribution delineated by the structure of the data. On the other hand,
600 a Gaussian mixture distribution can have any arbitrary arrangement of weighted components, which
601 makes the task of directly calculating the true local density mode for each embedded point both
602 analytically and numerically intractable. Therefore, to circumvent these problems, we apply the sparse
603 watershed assignment procedure described by Todd et al. (2017) to find the true local maximum for
604 each component in the distribution – rather than for every embedded observation – through numerical
605 optimization, which requires only a nominal amount of additional computation. We can then merge
606 overlapping components and assign embedded data to a mode that more accurately reflects the
607 underlying (potentially non-Gaussian) region of local density.

608 Because this sparse watershed procedure produces clusters with an arbitrary number of weighted
609 components, calculating the full posterior probability $p_{\theta}(\mathbf{y}|\mathbf{z})$ for each data point is computationally
610 complex. So for the sake of simplicity, we perform hard label assignment. In other words, we calculate
611 the mode of the cluster distribution for each value of \mathbf{z} , or:

$$l_i = \arg \max_l p_{\theta}(y_l | \mathbf{z}_i), \quad (5)$$

612 for $l = 1, \dots, K$, where l_i is the assigned label for the latent vector \mathbf{z}_i . This hard label assignment
613 procedure is performed in 3 steps: **(1)** latent vectors are initially assigned to the nearest (highest local
614 density) component in the Gaussian mixture prior; **(2)** the Gaussian mixture distribution is further
615 optimized to combine overlapping mixture components using sparse watershed assignment (Todd et al.,
616 2017); and **(3)** the initial cluster assignments are then recursively updated using the learned hierarchy of
617 overlapping components to ensure each latent vector is assigned to the mode that best represents the
618 underlying density of the local neighborhood for that observation. To accomplish these steps, the
619 expected value of the approximate posterior for each data point is initially assigned to a single mode in
620 the Gaussian mixture distribution by calculating the weighted mixture component with the maximum
621 likelihood (minimum distortion), which is written as:

$$k_i = \arg \max_k \omega_k \mathcal{N}(\mathbb{E}[q_{\phi}(\mathbf{z}|\mathbf{x}_i)] | \boldsymbol{\mu}_k, \mathbf{I}), \quad (6)$$

622 where k_i is the initial cluster assignment for the i th data point \mathbf{x}_i . We then combine degenerate
623 (highly-overlapping) modes from the distribution by applying the sparse watershed procedure described
624 by Todd et al. (2017). Using this procedure, the initial cluster assignments are further combined by
625 optimizing the mean of each component to ascend to its local maximum within the Gaussian mixture
626 prior, which we write as a minimization of the negative log-likelihood, or:

$$\mathbf{M}^* = \arg \min_{\mathbf{M}} -\frac{1}{K} \sum_{k=1}^K \log \sum_{l=1}^K \omega_l \mathcal{N}(\boldsymbol{\mu}_k | \boldsymbol{\mu}_l, \mathbf{I}), \quad (7)$$

627 where $\boldsymbol{\mu}_k^* \in \mathbf{M}^*$ is the optimized mean of each component. We optimize this objective numerically with
628 the Adam optimizer (Kingma and Ba, 2014) with a learning rate of 1×10^{-3} until the objective (Eq. 7)
629 stops improving for 100 training steps. We then merge cluster assignments based on whether the mode
630 for the initial cluster assignment k_i has moved within the basin of attraction for another mixture
631 component in the distribution (after optimizing Eq. 7), or:

$$l_i = \arg \max_l \omega_l \mathcal{N}(\boldsymbol{\mu}_{k_i}^* | \boldsymbol{\mu}_l, \mathbf{I}) \quad (8)$$

632 where l_i is the sparse watershed label assignment for the i th data point \mathbf{x}_i , which was assigned to the
633 k_i th mode of the distribution μ_{k_i} in the initial cluster assignment step (Eq. 6). We then repeat this
634 assignment procedure K times to ensure all label assignments to degenerate modes are reassigned to
635 the mode with the highest local density:

$$l_i := \arg \max_l \omega_l \mathcal{N}(\mu_{l_i}^* | \mu_l, \mathbf{I}) \text{ for } k = 1, \dots, K. \quad (9)$$

636 Note that, for data assigned to non-degenerate modes in the initial step, typically the cluster assignment
637 remains unchanged, where $l_i = k_i$.

638 4.2 Comparing dimensionality reduction algorithms

639 We compared VAE-SNE to other dimensionality reduction algorithms including PCA (scikit-learn v0.23.0;
640 Pedregosa et al. 2011), t-SNE (van der Maaten and Hinton, 2008), UMAP (v0.4.0; McInnes et al. 2018),
641 scvis (Ding et al., 2018), and ivis (v1.7.2; Szubert et al. 2019). Our main comparisons involve compressing
642 data to two dimensions for visualization purposes, but VAE-SNE (and other algorithms) can be used for
643 dimensionality reduction more generally.

644 4.2.1 openTSNE and t-SNE variants

645 For t-SNE we used the openTSNE (v0.4.0) implementation from Poličar et al. (2019), which includes
646 improvements from van der Maaten (2014); Linderman et al. (2017, 2019) to maximize speed and
647 scalability, as well as methods for embedding out-of-sample data described by Poličar et al. (2019) (see
648 also Berman et al. 2014; Kobak and Berens 2019). We tested two versions of openTSNE using both the
649 Barnes-Hut approximation (Barnes-Hut-SNE) from van der Maaten (2014) and the Fourier interpolation
650 approximation (Fit-SNE) from Linderman et al. (2017, 2019). However, Fit-SNE, the fastest version of
651 openTSNE, is practically limited to very low dimensional embeddings (i.e., 1-D or 2-D) due to the Fourier
652 interpolation algorithm used for approximating the gradient during optimization, and therefore cannot be
653 used for more general-purpose dimensionality reduction (Linderman et al., 2017, 2019).

654 4.2.2 scvis as a special case of VAE-SNE

655 We found the original implementation of scvis (Ding et al., 2018) difficult to use for our comparisons
656 without extensive modification, as it relies on outdated software dependencies and is limited to specific
657 data file formats for using the code. However, scvis (Ding et al., 2018) can be considered a special case
658 of VAE-SNE with specific hyperparameter settings, so instead we used VAE-SNE with hyperparameters
659 matched to those described by Ding et al. (2018) for making comparisons. In particular, we used the
660 network architecture for the encoder and decoder networks described by Ding et al. (2018), along with
661 ELU activations (Clevert et al., 2015). We also use the asymmetric similarity kernel for the
662 high-dimensional similarities (Eq. 17a), and we set $K = 1$ for the number of components in the prior
663 distribution (Eq. 2). For benchmarking the processing speed of scvis (Ding et al., 2018), we disabled our
664 added parallel computations (Section 4.5) to match the speed of the original implementation from Ding
665 et al. (2018), and we calculated training time based on the original recommendation from Ding et al.
666 (2018) for training with batch size of 512 for 100 epochs.

667 4.2.3 Setting hyperparameters for comparisons

668 For each algorithm we used Euclidean distances for calculating pairwise similarities (the default for all
669 of the algorithms tested) along with the default settings for all other hyperparameters with some
670 exceptions. For t-SNE, we set `n_jobs=-1` to enable parallel processing. For UMAP, we also compare PCA
671 initialization for the low-dimensional embedding (vs. the default Laplacian Eigenmap initialization),
672 which is not a default option but improves global structure preservation. For ivis (Szubert et al., 2019),

673 we used the default model and followed recommendations from Szubert et al. (2019) to adjust the early
674 stopping criteria for different dataset sizes.

675 The hyperparameters for different methods could, of course, be adjusted ad infinitum to produce
676 different types of embeddings and could bias performance for different datasets in many ways; however,
677 the comparisons we make in this paper are not meant to be exhaustive, only informative in terms of
678 validating VAE-SNE as a comparable method. In the end, researchers will have to decide for themselves
679 which algorithm is most useful for their specific application. It is also worth considering that, for some
680 of the algorithms tested, adjusting the hyperparameters can dramatically alter computational and
681 memory requirements – for example, increasing the perplexity hyperparameter for Flt-SNE (Linderman
682 et al., 2017) and Barnes-Hut-SNE (van der Maaten, 2014) or the `n_neighbors` hyperparameter for UMAP,
683 increases number of nearest neighbors that are computed and, consequently, the size of the nearest
684 neighbors graph used to optimize the embedding. Our decision to use default settings is also especially
685 reasonable for the t-SNE variants we tested given that the openTSNE package (Poličar et al., 2019) uses
686 hyperparameter suggestions from Kobak and Berens (2019), which have been empirically shown to work
687 well across many datasets.

688 4.2.4 VAE-SNE hyperparameters

689 We tested multiple variants of VAE-SNE in our comparisons, but across these variants we use similar
690 hyperparameters for training. For the encoder and decoder networks we use 4 densely-connected layers
691 each with 256 units (with biases). For each layer we apply the nonlinear SELU activation function and
692 use the appropriate random initialization for the weights described by Klambauer et al. (2017). We train
693 each VAE-SNE model for a maximum of 100 epochs with an initial batch size of 512 using the Adam
694 optimizer (Kingma and Ba, 2014) with a learning rate of 0.001. For the perplexity hyperparameter, we
695 calculate this as a function of the batch size used during training, which we call the *perplexity ratio*, such
696 that $P = b\varrho$ where P is the perplexity, b is the batch size, and ϱ is the perplexity ratio. To improve global
697 structure preservation, we begin training with $\varrho = 0.1$ and then anneal to $\varrho = 0.01$ by exponentially
698 decaying ϱ after each training batch (similar to the perplexity annealing technique described by Kobak
699 and Berens 2019). After the perplexity ratio is fully annealed to the target value, we then perform early
700 stopping if pairwise similarity loss stops improving by at least 0.001 per epoch with a patience of 5
701 epochs (lack of progress is ignored for 5 epochs before stopping training). While it is common practice
702 to decrease the learning rate after training stagnates to further improve performance, we instead
703 increase the batch size, which has been shown to provide similar improvements (Smith et al., 2017).
704 Therefore after training stagnates and early stopping is initiated for the initial batch size of 512, we
705 increase the batch size to 1024 and continue training until early stopping is initiated again using the
706 same criteria. For the Gaussian mixture prior we set the number of components to $K = 100$, but we
707 found that any arbitrarily large number of components produced similar (nearly identical) results.

708 We tested 4 variants of VAE-SNE with different similarity kernels. We tested VAE-SNE using a t-SNE
709 similarity kernel with (1) constant kernel parameters ($\nu = \tau = 1$) as well as (2) learned kernel parameters
710 (van der Maaten, 2009). We also tested VAE-SNE variants using a SNE kernel with (3) constant ($\eta = 1$)
711 and (4) learned parameters as well. Otherwise the hyperparameters for each variant were kept constant,
712 as described above.

713 4.2.5 Local structure preservation

714 After embedding the data with each algorithm we assessed local structure preservation with two
715 measures of preservation that define local neighborhoods in different ways. For both of these metrics
716 we targeted neighborhoods that correspond to $\sim 1\%$ of the total embedding size.

717 **metric-based neighborhoods** First, we used a metric-based measure of local neighborhood
718 preservation, where neighborhoods are defined based on distance (a fixed radius) to a cluster center.
719 Following Becht et al. (2019) we applied the k-means clustering algorithm (with $k = 100$ clusters; using

720 scikit-learn v0.23; Pedregosa et al. 2011) to the high-dimensional data and the low-dimensional
721 embedding for each method, which effectively divides the data into small Voronoi regions. We then
722 calculated the normalized mutual information (reviewed by Vinh et al. 2010; see also McDaid et al. 2011)
723 between the high-dimensional and low-dimensional cluster assignments (using scikit-learn v0.23;
724 Pedregosa et al. 2011). This provides a symmetric and permutation invariant measure of how well local
725 neighborhood memberships from the high-dimensional space are preserved by each embedding method
726 – with similarity ranging from 0 (no overlap, or random) to 1 (perfect overlap). We performed 5 replicates
727 of this for each trial.

728 **topological neighborhoods** Second, we assessed local neighborhood preservation topologically by
729 calculating the exact nearest neighbors for 1000 randomly selected data points and then defining the
730 local neighborhood for each point as k nearest neighbors, where k is selected such that $\frac{k}{N} \approx 0.01$, and
731 N is the total embedding size. We then computed the proportion of the neighbors that are assigned to
732 the correct local neighborhood in low-dimensional embedding, which ranges from 0 (no neighbors
733 preserved) to 1 (all neighbors preserved). We performed 5 replicates of this for each trial.

734 4.2.6 Global structure preservation

735 To assess global structure preservation we follow Becht et al. (2019) by calculating the Pearson
736 correlation between pairwise squared Euclidean distances for 10,000 points in the high-dimensional
737 space and the low-dimensional embedding for each method (for a total of 49.995 million distances). As
738 distances have a lower bound of zero and tend to follow a log-normal (or Gamma) distribution, we first
739 log transformed the distances in order to homogenize the variance and better match the assumptions of
740 Pearson's correlation score. The Pearson correlation then provides a measure of the global structure
741 preservation ranging from -1 (anti-correlated) to 1 (correlated). We performed 5 replicates of this for
742 each trial.

743 4.2.7 Fine-scale structure preservation

744 Because our metrics for local structure preservation only account for a single scale but not the
745 fine-scale structure within local neighborhoods, we also assessed topological structure preservation for
746 smaller neighborhood sizes. As before, we calculated the exact nearest neighbors for 1000 randomly
747 selected data points. We then computed the proportion of points assigned to the correct neighborhood
748 across 14 dyadically (\log_2) spaced neighborhood sizes ranging from $k = 2^1$ to $k = 2^{14}$. Neighborhood
749 sizes were then normalized as a proportion of the total embedding size, or $\frac{k}{N}$. We performed 5 replicates
750 of this for each trial and neighborhood size.

751 4.2.8 Temporal structure preservation

752 Because the largest dataset we use is also timeseries data, we assess temporal structure preservation
753 for the test set by calculating Euclidean distances between sequential time points in high-dimensions
754 and low-dimensions for each method. We then calculate the Pearson correlation coefficient of the log
755 transformed distances (same as for assessing global structure preservation) for 50 randomly selected
756 10 minute subsets (60,000 observations) within the full timeseries. This then provides a measure of how
757 well temporal derivatives are preserved in the low-dimensional embedding ranging from -1
758 (anti-correlated) to 1 (correlated).

759 4.2.9 Hierarchical bootstrap for statistical comparisons

760 To compare each information preservation metric statistically we performed hierarchical bootstrapping
761 (see Saravanan et al. 2019 for a recent review). Every trial for each dimension reduction method has
762 multiple observations per metric, which creates hierarchical dependencies in the data. To account for

763 this, we use seaborn v0.10.1 (Waskom et al., 2020) to calculate and plot hierarchical bootstrap estimates
764 of the mean for each information preservation metric – resampling (with replacement) both within trials
765 and across trials ($n=1000$ bootstrap samples). We then plot the 95% intervals of the bootstrap
766 distribution to compare the performance of each dimension reduction method statistically. Rather than
767 attempting to make decisions regarding the statistical “significance” of these bootstrap distributions
768 based on an arbitrary threshold, we instead simply treat them as a measure of the uncertainty (variance)
769 in effect size for each information preservation metric. The computational experiments from which the
770 information preservation metrics are derived could be run ad infinitum to achieve statistical significance,
771 which is effectively a measure of statistical resolution based on the number of observations, but this is
772 not necessarily informative in practice.

773 4.3 Datasets

774 4.3.1 Animal body posture dynamics

775 The largest dataset we used for comparisons is a behavioral dataset from Berman et al. (2014, 2016);
776 Pereira et al. (2019) consisting of ~ 1 -h video recordings (at 100Hz) for 59 freely-behaving individual fruit
777 flies (*Drosophila melanogaster*) for a total of ~ 21.1 million observations (downloaded from:
778 <http://arks.princeton.edu/ark:/88435/dsp01pz50gz79z>). We tracked the full body posture of each
779 individual with DeepPoseKit v0.3.6 (Graving et al., 2019) using the procedures described by Graving et al.
780 (2019) to train a deep convolutional pose estimation model using the keypoint annotations from Pereira
781 et al. (2019) as training data. For each video this produced a multivariate time series of the Euclidean
782 coordinates describing 32 body part positions in the video – including the head, neck, eyes, thorax,
783 abdomen, wings, and 24 leg joints. We then rotationally and translationally aligned the posture data at
784 each timepoint to the major body axis (neck-thorax vector) and calculated the sine and cosine of the
785 keypoint angles for the 30 body parts not used for alignment. This resulted in a $30 \times 2 = 60$ dimensional
786 posture timeseries. To transform the spatial posture data into a dynamical spatio-temporal
787 representation, we then applied a normalized Morlet wavelet transform from Berman et al. (2014) using
788 the behavelt Python package v0.0.1 (Graving, 2019) to generate a multi-scale time-frequency
789 spectrogram of the body posture dynamics for each time point. Following Berman et al. (2014); Pereira
790 et al. (2019), we used 25 dyadically (\log_2) spaced frequencies ranging from 1Hz to 50Hz (the Nyquist
791 frequency of the signal), which expanded the dimensionality of the timeseries from $30 \times 2 = 60$ to
792 $30 \times 2 \times 25 = 1500$.

793 **Dimension reduction comparisons** To generate a training set for benchmarking the different
794 algorithms, we uniformly randomly sampled a subset of data from the body posture dynamics timeseries
795 for 58 of 59 individuals while excluding one randomly selected individual to use as a test set. We tested
796 4 training set sizes: $58 \times 500 = 29,000$; $58 \times 1000 = 58,000$; $58 \times 2000 = 116,000$; $58 \times 4000 = 232,000$,
797 above which we encountered out-of-memory errors when running UMAP (McInnes et al., 2018) on larger
798 subsets of data. Each test set contains $\sim 360,000$ sequential observations. We then applied each
799 dimension reduction method to the training set and subsequently embedded the test set. For training
800 VAE-SNE we used the cross-entropy loss as a log likelihood function, as it matches well with the
801 normalized time-frequency data, but we also found that other likelihood functions work similarly well.

802 **Behavioral clustering** To simplify the dataset for performing our clustering analysis, we used the sine
803 and cosine of the keypoint angles for the 6 legs (the distal tips of each leg), 2 wings, head, and abdomen
804 for a total of 10 body parts and a $10 \times 2 = 20$ dimensional posture timeseries. As before we applied the
805 time-frequency transform which expands the dimensionality of the timeseries from $10 \times 2 = 20$ to
806 $10 \times 2 \times 25 = 500$. We then applied VAE-SNE with a t-SNE kernel (Appendix B; $\nu = \tau = 1$) to compress
807 the spectrogram data to 30 dimensions. We used the cross-entropy between normalized time-frequency
808 vectors, or $\mathbb{H}[\mathbf{x}_i, \mathbf{x}_j] = -\sum \mathbf{x}_i \log \mathbf{x}_j$, as our metric for calculating high-dimensional similarities
809 (Appendix B), as this provides a more natural measure of divergence between the normalized

810 spectrograms than Euclidean distance. The cross-entropy is closely related (up to a constant) to the
811 Kullback-Leibler divergence — the metric originally used by Berman et al. (2014) — but is slightly faster to
812 calculate, which reduces training time. When visualizing the spectrograms we integrate (sum) across
813 the wavelet coefficients for the sine and cosine for each body part in the spectrogram.

814 **4.3.2 Single-cell RNA-seq**

815 To test the application of VAE-SNE to single-cell RNA-seq data, we used data from La Manno et al. (2018)
816 which consists of 18,213 observations describing the development and cell fate of hippocampal neurons.
817 We preprocessed these data using the `velocity.py` (v0.17.17) package from La Manno et al. (2018). We
818 compressed the raw expression values to 500 dimensions using PCA before applying subsequent
819 dimension reduction algorithms. We applied each dimension reduction algorithm to the full dataset and
820 then re-embedded the training set in place of a test set in order to evaluate the speed for embedding new
821 data. We report information preservation metrics only for the training set, as no test set was used due to
822 the relatively small size of the dataset. For training VAE-SNE on this dataset we use a Student-t
823 likelihood function, but found other likelihood functions work similarly well.

824 **4.3.3 Natural history images**

825 We also applied a convolutional variant of VAE-SNE to natural history images, and to test this we used
826 two datasets: a set of 59,244 shell images from Zhang et al. (2019) and a set of 2,468 butterfly images
827 from Cuthill et al. (2019). All images were preprocessed by applying local adaptive thresholding to detect
828 and remove the background. Images were then zero-padded to create a 1:1 aspect ratio and resized to a
829 resolution of 192×192 . We trained convolutional VAE-SNE using the same hyperparameters as the
830 dimension reduction experiments, but using batches of only 256 images.

831 **4.4 Computing hardware**

832 All performance comparisons were conducted on a high-end consumer-grade workstation equipped with
833 an Intel Core-i9-7900X CPU (10 cores, 20 threads @ 3.30GHz), 32GB of DDR4 RAM, a 4TB NVMe solid
834 state drive, and a NVIDIA GeForce GTX 1080 Ti GPU (11 GB GDDR5X VRAM).

835 **4.5 Parallelizing pairwise computations to improve performance**

836 To improve performance of pairwise computations over Ding et al. (2018), we reimplemented the
837 underlying algorithms for training VAE-SNE. The largest performance bottleneck for VAE-SNE is the
838 recursive binary search algorithm for computing high-dimensional pairwise similarities (Appendix B).
839 However, the computations for this algorithm are embarrassingly parallel, so we reimplemented it to run
840 recursion loops in parallel across multiple CPU threads. This was accomplished by JIT-compiling the
841 code using the `numba` library (Lam et al., 2015), which resulted in massive speed improvements. We
842 also reimplemented all pairwise distance calculations on the GPU using PyTorch (Paszke et al., 2019),
843 which further improved performance.

844 **4.6 Code availability**

845 The code for VAE-SNE is freely available at <https://github.com/jgraving/vaesne> under a permissive
846 open-source license. The library is written primarily using PyTorch v1.5.0 (Paszke et al., 2019) and
847 includes a scikit-learn-style API (Buitinck et al., 2013) for fitting the model (`model.fit()`) and predicting
848 on new data (`model.predict()`).

849 **Acknowledgments**

850 We thank Gordon Berman and members of the Berman lab, Tim Landgraf, Ben Wild, David Dormagen,
851 Conor Heins, Blair Costelloe, Ian Etheredge, and Ari Strandburg-Peshkin for their helpful comments on
852 the manuscript. We are also grateful to Mike Costelloe for his creative advice on the figures, Einat
853 Couzin-Fuchs and Dan Bath for their expert input, and Michael Smith for the use of his GPU. J.M.G. and
854 I.D.C. acknowledge support from the Deutsche Forschungsgemeinschaft (DFG, German Research
855 Foundation) under Germany's Excellence Strategy - EXC 2117 - 422037984. I.D.C. acknowledges support
856 from NSF Grant IOS-1355061, Office of Naval Research Grant (ONR, N00014-19-1-2556), the Struktur-und
857 Innovationsfonds für die Forschung of the State of Baden-Württemberg, and the Max Planck Society.

858 **Competing Interests**

859 The authors declare no competing interests

860 **Author Contributions**

- 861 • **J.M.G.** – Conceptualization, Data curation, Software, Formal analysis, Validation, Investigation,
862 Visualization, Methodology, Writing–original draft, Project administration, Writing–review and
863 editing
- 864 • **I.D.C.** – Conceptualization, Resources, Writing–reviewing and editing, Supervision, Project
865 administration, Funding acquisition

866 **Supplemental Figures**

Table S1. Ranked information preservation metric performance for nonlinear dimension reduction algorithms. Rankings for each nonlinear dimension reduction algorithm in terms of general performance for local, global, fine-scale, and temporal structure preservation (lower is better).

name	citation	local	global	fine-scale	temporal
VAE-SNE (t-SNE)	this paper	1	1	2	2
VAE-SNE (SNE)	this paper	2	1	2	1
FIt-SNE	Linderman et al. (2017)	1	2	1	2
Barnes-Hut-SNE	van der Maaten (2014)	1	2	1	2
UMAP (LE init)	McInnes et al. (2018)	1	3	2	3
UMAP (PCA init)	McInnes et al. (2018)	1	2	2	3
scvis	Ding et al. (2018)	2	1	2	2
ivis	Szubert et al. (2019)	2	1	3	1

Table S2. Ranked processing speed performance for nonlinear dimension reduction algorithms. Rankings for each nonlinear dimension reduction algorithm in terms of general performance for training time and test time (lower is better), as well as whether or not test time increases as a function of training set size.

name	citation	train time	test time	test time \propto train size
VAE-SNE	this paper	4	1	no
FIt-SNE	Linderman et al. (2017)	2	4	no
Barnes-Hut-SNE	van der Maaten (2014)	3	5	yes
UMAP	McInnes et al. (2018)	1	3	yes
scvis	Ding et al. (2018)	6	1	no
ivis	Szubert et al. (2019)	5	2	no

Table S3. Additional features for nonlinear dimension reduction algorithms. A summary of potentially useful additional features for each nonlinear dimension reduction algorithm including batch training for applying dimension reduction to large out-of-core datasets, non-Euclidean embeddings for different types of compressed representations, whether the algorithm is tractable in higher dimensions (>2), and whether the algorithm learns a distribution of clusters within the data.

name	citation	batch training	non-Euclidean	>2 dims.	clustering
VAE-SNE	this paper	yes	yes	yes	yes
FIt-SNE	Linderman et al. (2017)	no	no	no	no
Barnes-Hut-SNE	van der Maaten (2014)	no	no	yes	no
UMAP	McInnes et al. (2018)	no	yes	yes	no
scvis	Ding et al. (2018)	yes	no	yes	no
ivis	Szubert et al. (2019)	yes	no	yes	no

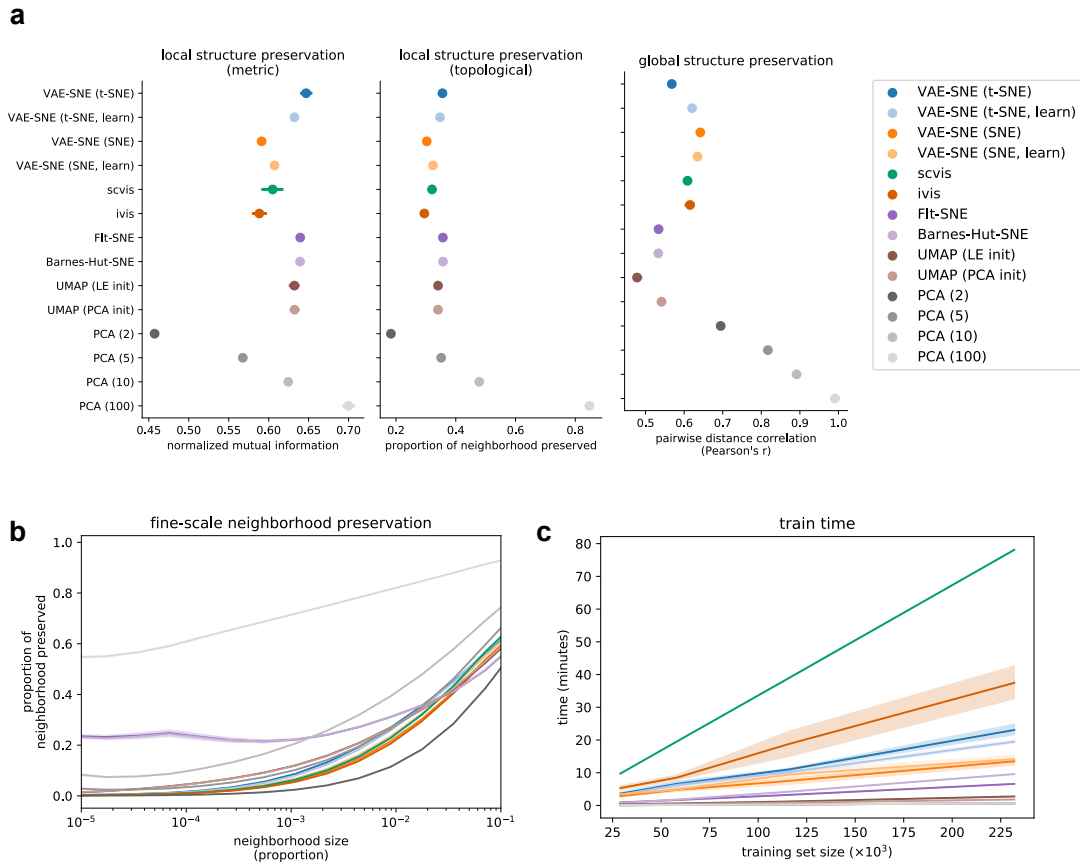


Figure S1. Dimension reduction performance for the posture dynamics training set. Plots show performance comparisons for the posture dynamics dataset (Berman et al., 2014, 2016; Pereira et al., 2019) using the training set. **a**, Mean and 95% interval of the bootstrap distribution for local and global structure preservation. Results are pooled across all training set sizes (for each metric $n = 4$ training set sizes \times 5 trials \times 5 replicates = 100 per algorithm). **b**, Mean and 95% interval of the bootstrap distribution for fine-scale structure preservation across multiple neighbor sizes (as a proportion of the total embedding size). Results are from the largest training set size only ($n = 14$ neighborhood sizes \times 5 trials \times 5 replicates = 350 per algorithm). **c**, Training time for fitting each algorithm across different training set sizes ($n = 4$ training set sizes \times 5 trials = 20 per algorithm).

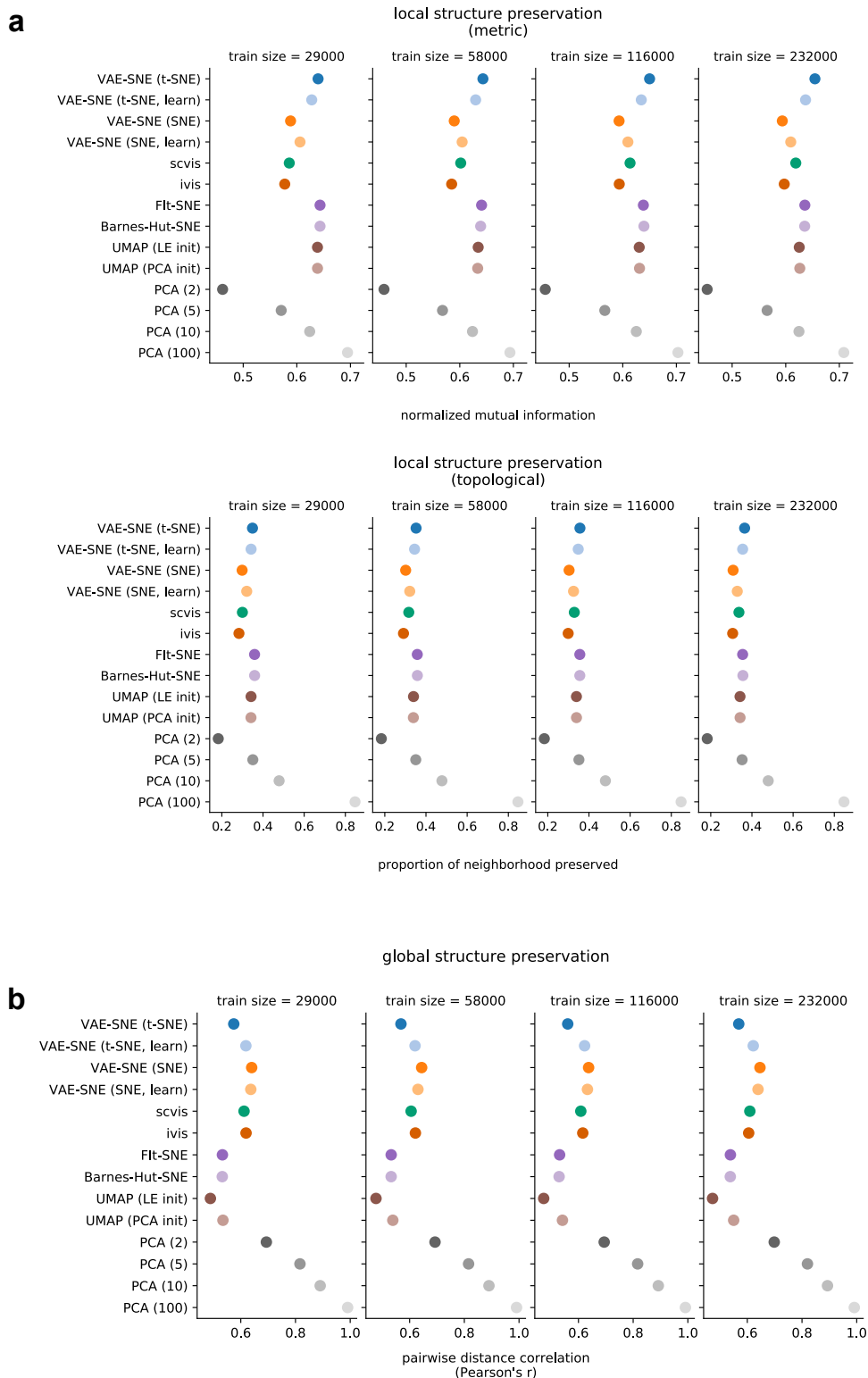


Figure S2. Dimension reduction performance for the posture dynamics training set across training set sizes. Plots show performance comparisons for the posture dynamics dataset (Berman et al., 2014, 2016; Pereira et al., 2019) using training sets of different sizes. **a-b**, Mean and 95% interval of the bootstrap distribution for local (**a**) and global (**b**) structure preservation. (for each metric $n = 5 \text{ trials} \times 5 \text{ replicates} = 25$ per training set size per algorithm)

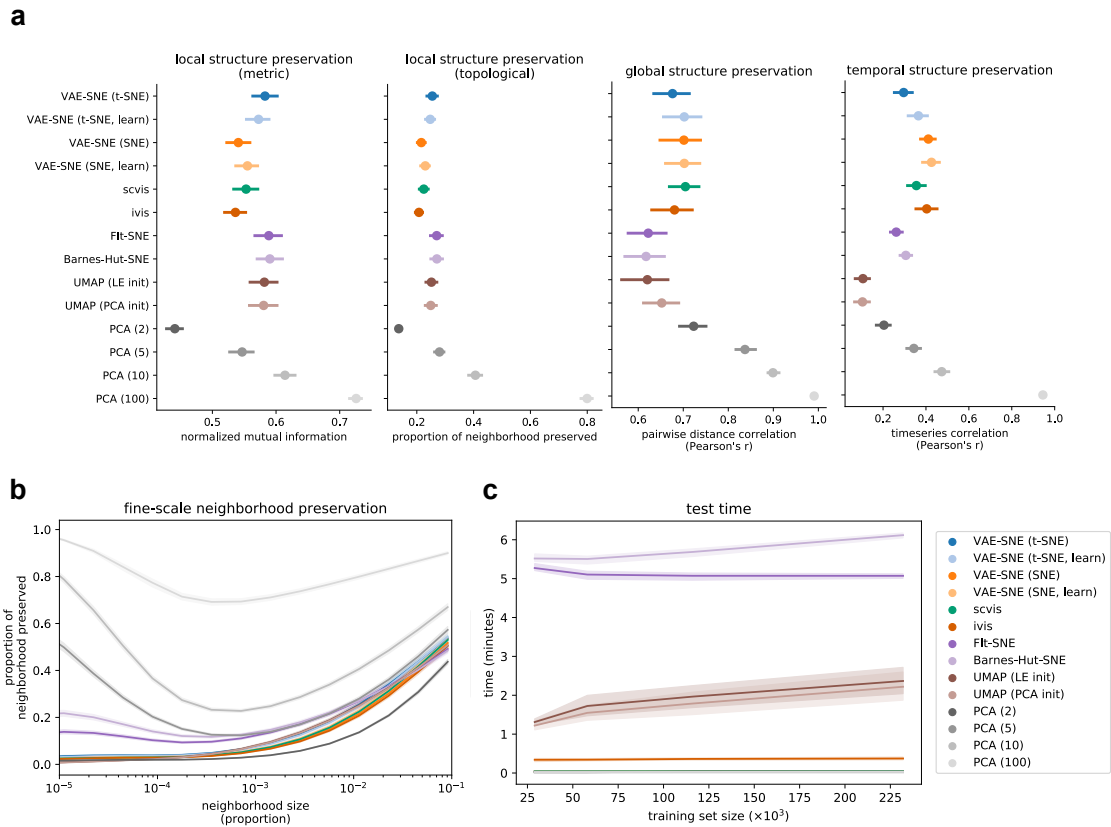


Figure S3. Dimension reduction performance for the posture dynamics test set. Plots show performance comparisons for the posture dynamics dataset (Berman et al., 2014, 2016; Pereira et al., 2019) using the test set. **a**, Mean and 95% interval of the bootstrap distribution for local, global, and temporal structure preservation. Results are pooled across all training set sizes (for local and global structure $n = 4$ training set sizes $\times 5$ trials $\times 5$ replicates = 100 per algorithm; for temporal structure $n = 4$ training set sizes $\times 5$ trials $\times 50$ subsamples = 1000 per algorithm). **b**, Mean and 95% interval of the bootstrap distribution for fine-scale structure preservation across multiple neighbor sizes (as a proportion of the total embedding size). Results are from the largest training set size only ($n = 14$ neighborhood sizes $\times 5$ trials $\times 5$ replicates = 350 per algorithm). **c**, Elapsed time for embedding the test set with each algorithm across different training set sizes ($n = 4$ training set sizes $\times 5$ trials = 20 per algorithm).

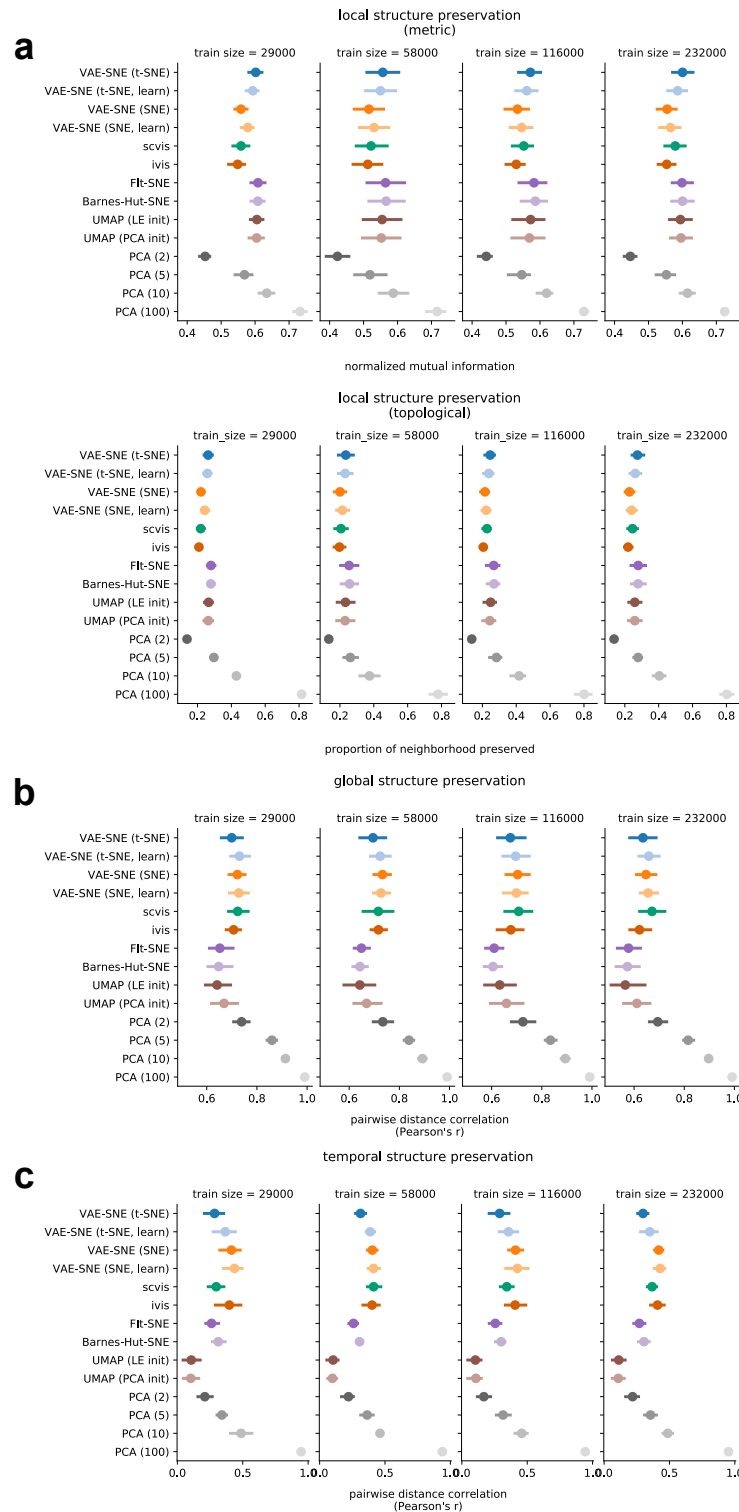


Figure S4. Dimension reduction performance for the posture dynamics test set across training set sizes. Plots show performance comparisons for the posture dynamics dataset (Berman et al., 2014, 2016; Pereira et al., 2019) using training sets of different sizes. **a-c**, Mean and 95% interval of the bootstrap distribution for local (**a**), global (**b**), and temporal (**c**) structure preservation (for local and global structure $n = 5 \text{ trials} \times 5 \text{ replicates} = 25$ per algorithm for each training set size; for temporal structure $n = 5 \text{ trials} \times 50 \text{ subsamples} = 250$ per algorithm for each training set size).

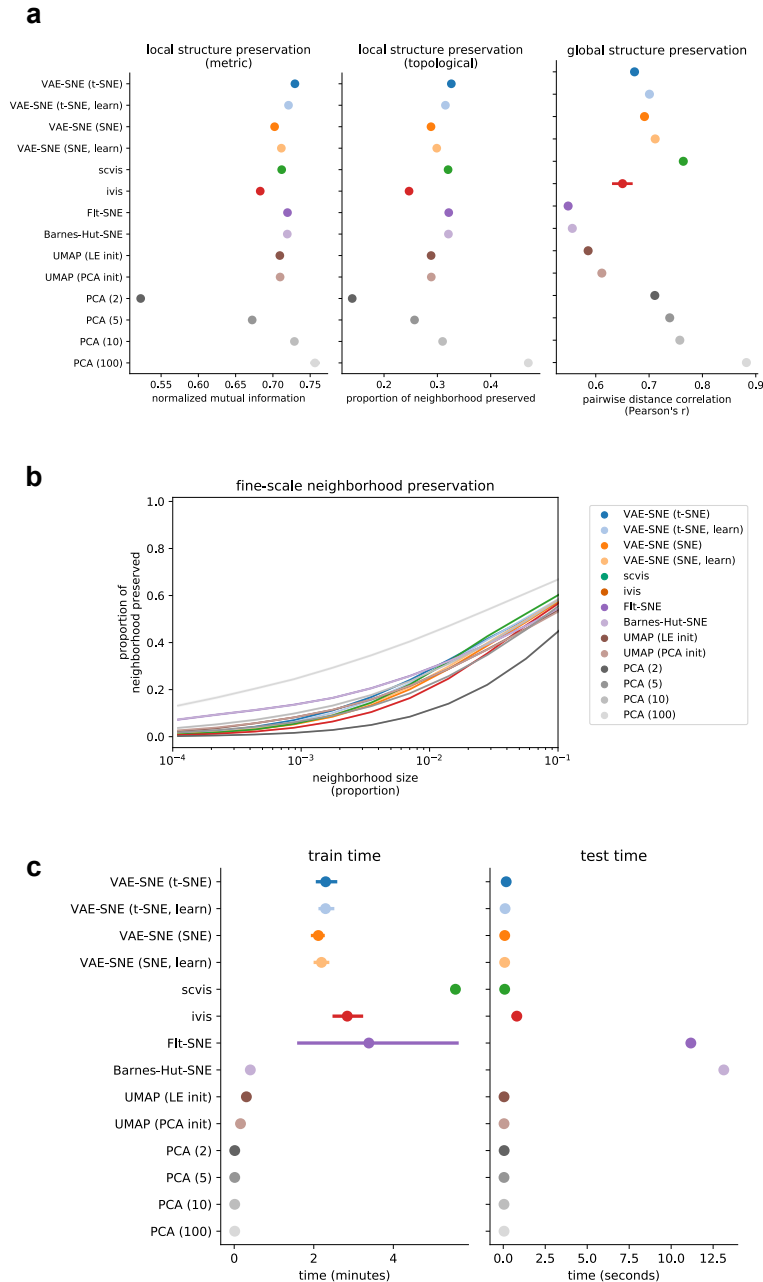


Figure S5. Dimension reduction performance for the single-cell RNA-seq dataset. Plots show performance comparisons for the single-cell RNA-seq dataset from La Manno et al. (2018) using the entire dataset. **a**, Mean and 95% interval of the bootstrap distribution for local and global structure preservation (for each metric $n = 5 \text{ trials} \times 5 \text{ replicates} = 25$ per algorithm). **b**, Mean and 95% interval of the bootstrap distribution for fine-scale structure preservation across multiple neighbor sizes (as a proportion of the total embedding size; $n = 14 \text{ neighborhood sizes} \times 5 \text{ trials} \times 5 \text{ replicates} = 350$ per algorithm). **c**, Elapsed time for embedding the training set and re-embedding the training set as a “test” set with each algorithm (for each metric $n = 5 \text{ trials} \times 5 \text{ replicates} = 25$ per algorithm).

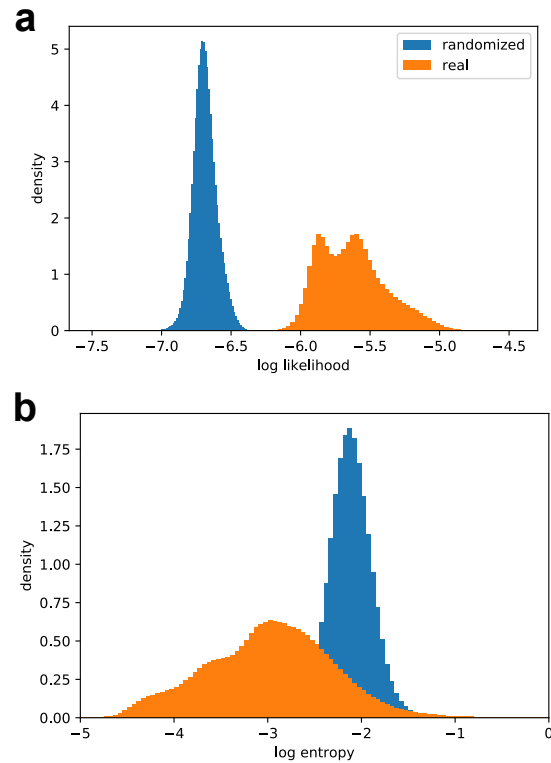


Figure S6. Likelihood and entropy distributions. **a**, Histograms of the log likelihood scores from the decoder (Eq. 1b; distortion) for real and randomized data ($n = 232,000$ for each distribution). **b**, Histograms of the log entropy from the approximate posterior (Eq. 12d) for real and randomized data ($n = 232,000$ for each distribution).

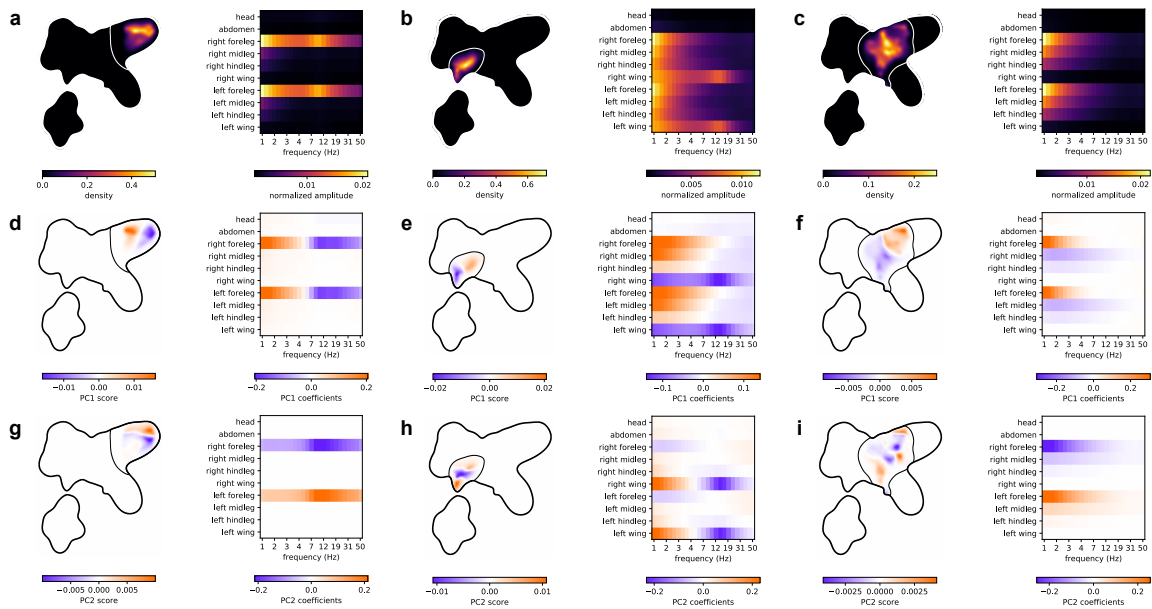


Figure S7. High-level behavioral clusters. Visualizations describing the manually-grouped high-level clusters for anterior grooming (**a,e,g**), wing movements (**b,e,h**) and small/slow leg movements (**c,f,i**). **a-c**, The 2-D posterior probability density for each cluster (left), where contours are the largest 90% probability density contour for each cluster distribution, and the mean spectrogram for each cluster (right). **d-i**, The principal component scores of the spectrograms assigned to each cluster visualized within the 2-D embedding (left) and the eigenvector coefficients describing the linear contribution of each spectrogram feature (right) for the principal component score.

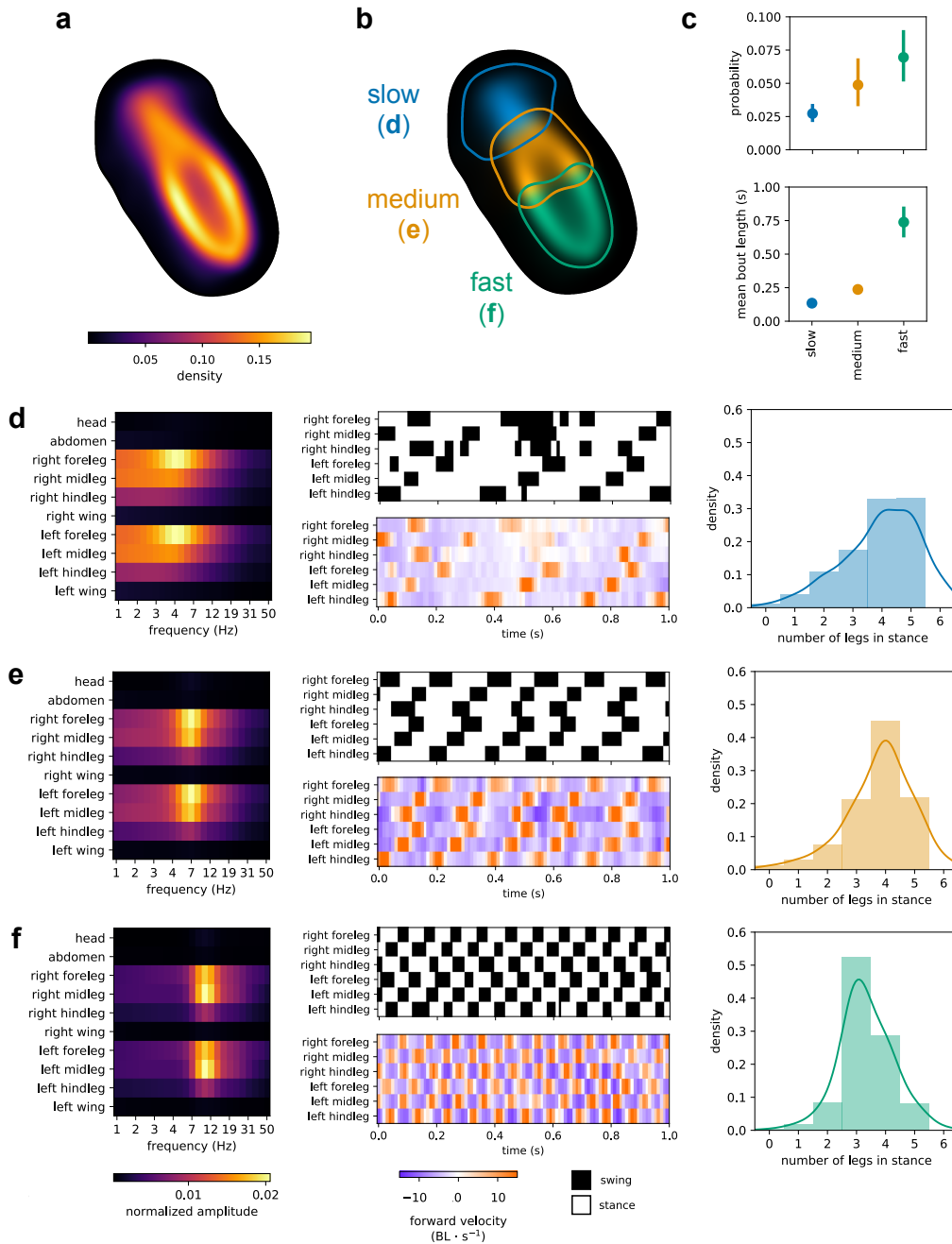


Figure S8. Low-level locomotion clusters. Visualizations describing the low-level clusters within the high-level locomotion cluster. **a-b**, The 2-D posterior probability density for the high-level cluster (**a**) and for each low-level cluster (**b**), where letters for each cluster label correspond to panels **d-f**. Contours are the largest 90% probability density contour for each cluster distribution. **c**, Mean and 95% bootstrap intervals of the marginal (stationary) probability and mean bout length for each low-level cluster ($n = 59$ per cluster). **d-f**, The mean spectrogram (left), example time segments (middle) showing forward velocity of each leg measured in body lengths (BL) per second and swing (forward velocity $> 0 \text{ BL} \cdot \text{s}^{-1}$) or stance (forward velocity $\leq 0 \text{ BL} \cdot \text{s}^{-1}$) classification, and histograms (right) showing the number of legs classified as stance in each timestep assigned to each cluster ($n = 0.57$ million for slow, **d**; $n = 1.03$ million for medium, **e**; and $n = 1.47$ million for fast, **f**) – where the label for each panel in **d-f** corresponds to a cluster label in panel **b**. Example videos for these low-level clusters are shown in Video S2.

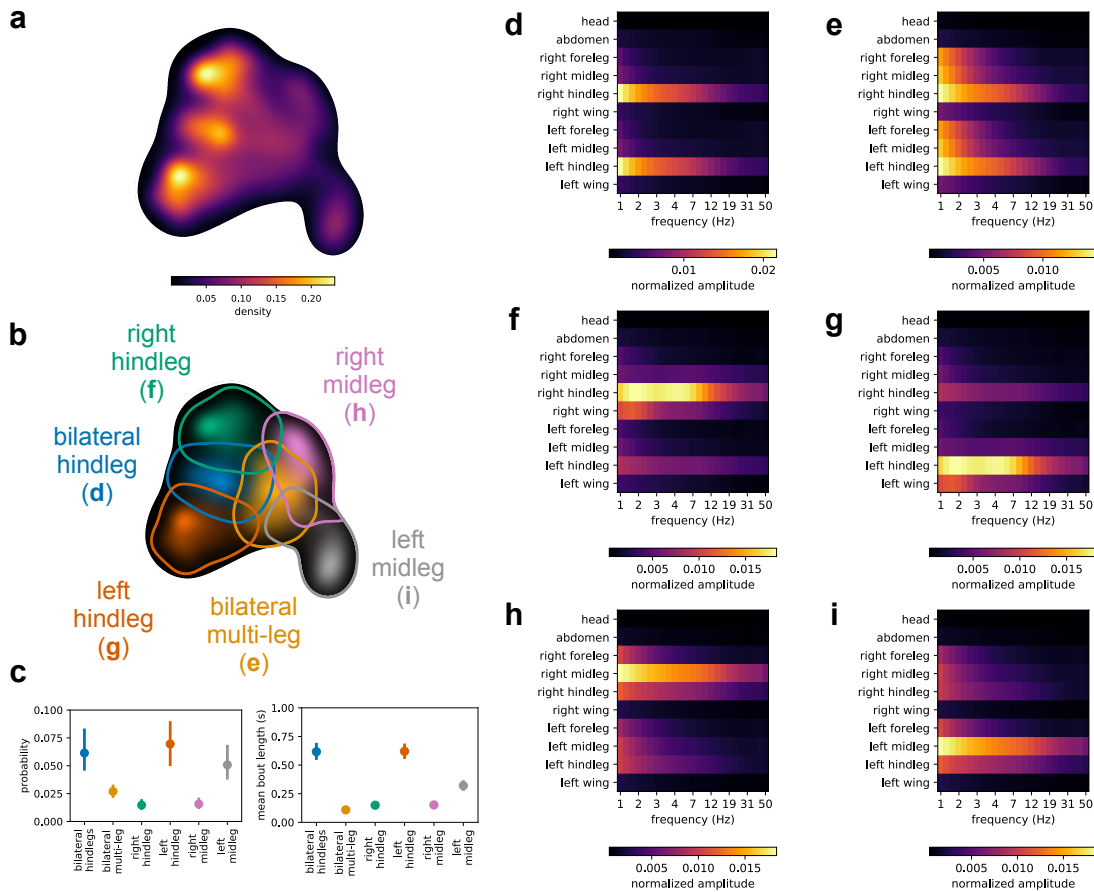


Figure S9. Low-level posterior grooming clusters. Visualizations describing the low-level clusters within the high-level posterior grooming cluster. **a-b**, The 2-D posterior probability density for the high-level cluster (**a**) and for each low-level cluster (**b**), where letters for each cluster label correspond to panels **d-i**. Contours are the largest 90% probability density contour for each cluster distribution. **c**, Mean and 95% bootstrap intervals of the marginal (stationary) probability and mean bout length for each low-level cluster ($n = 59$ per cluster). **d-i**, The mean spectrogram for each cluster – where the label for each panel in **d-i** corresponds to a cluster label in panel **b**. Example videos for these low-level clusters are shown in Video S4.

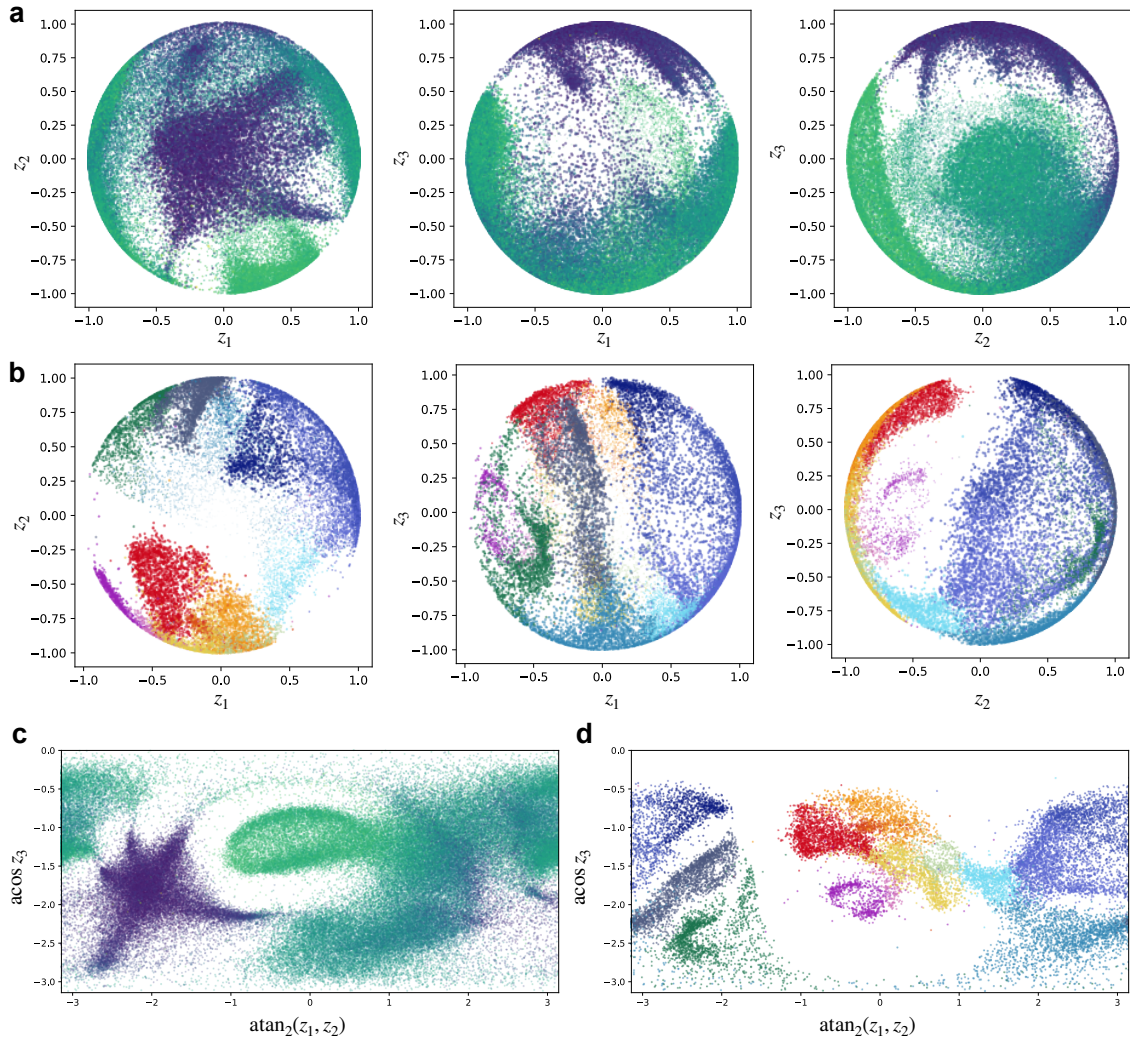


Figure S10. Spherical embeddings with von Mises-Fisher VAE-SNE. **a-b**, Spherical embeddings using VAE-SNE with a von Mises-Fisher similarity kernel (Appendix C.1) of the posture dynamics dataset (**a**; Video S8) from Berman et al. (2014, 2016); Pereira et al. (2019) and the single-cell RNA-seq dataset (**b**; Video S9) from La Manno et al. (2018). **c-d**, Stereographic (planar) projections of the spherical embeddings from **a-b**. Colors for **a-d** are the same as in Fig. 2 (total amplitude and cell type).

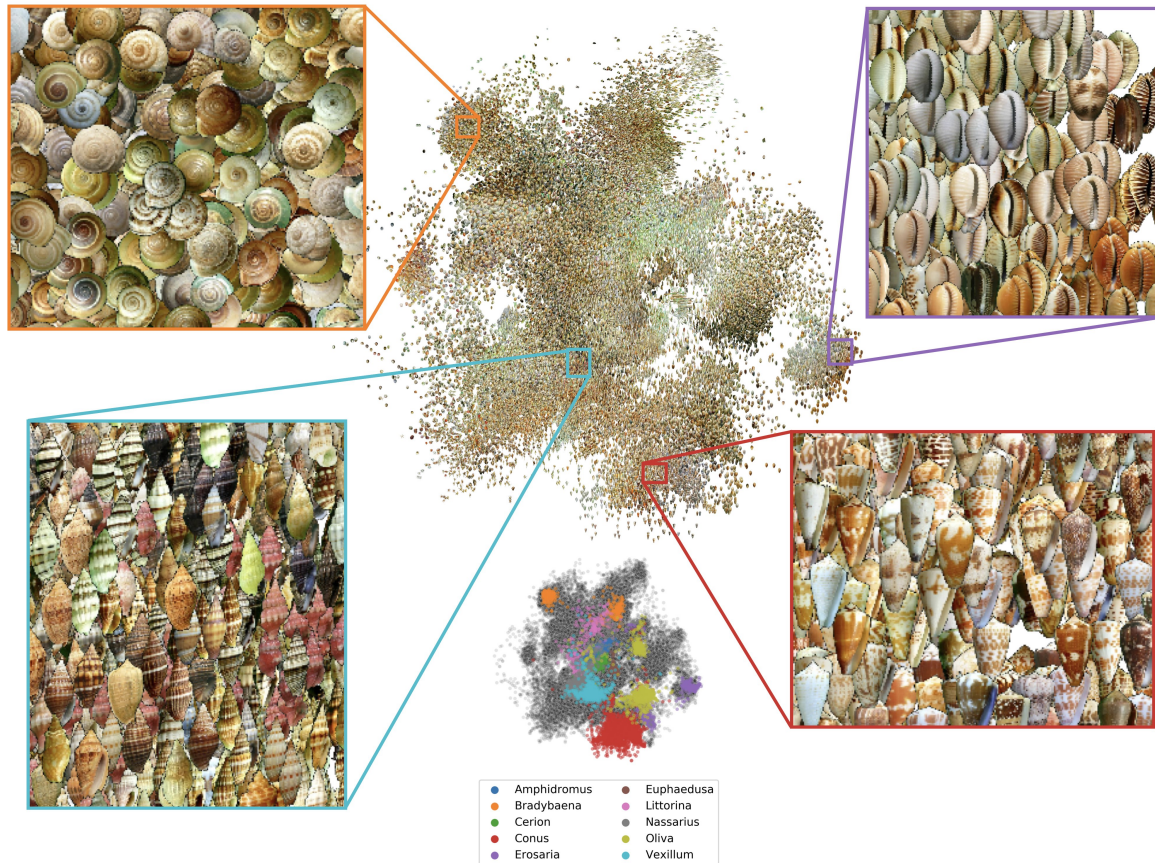


Figure S11. Embedding shell images. Shell images from Zhang et al. (2019) embedded in two dimensions using convolutional VAE-SNE. Insets illustrate example regions of perceptually similar images from the taxonomic genera *Bradybaena* (land snails; top-left), *Erosaria* (cowries; top-right), *Vexillum* (sea snails; bottom-left), and *Conus* (cone snails; bottom-right). Scatter plot (bottom-center) shows the 10 most common genera in the dataset.

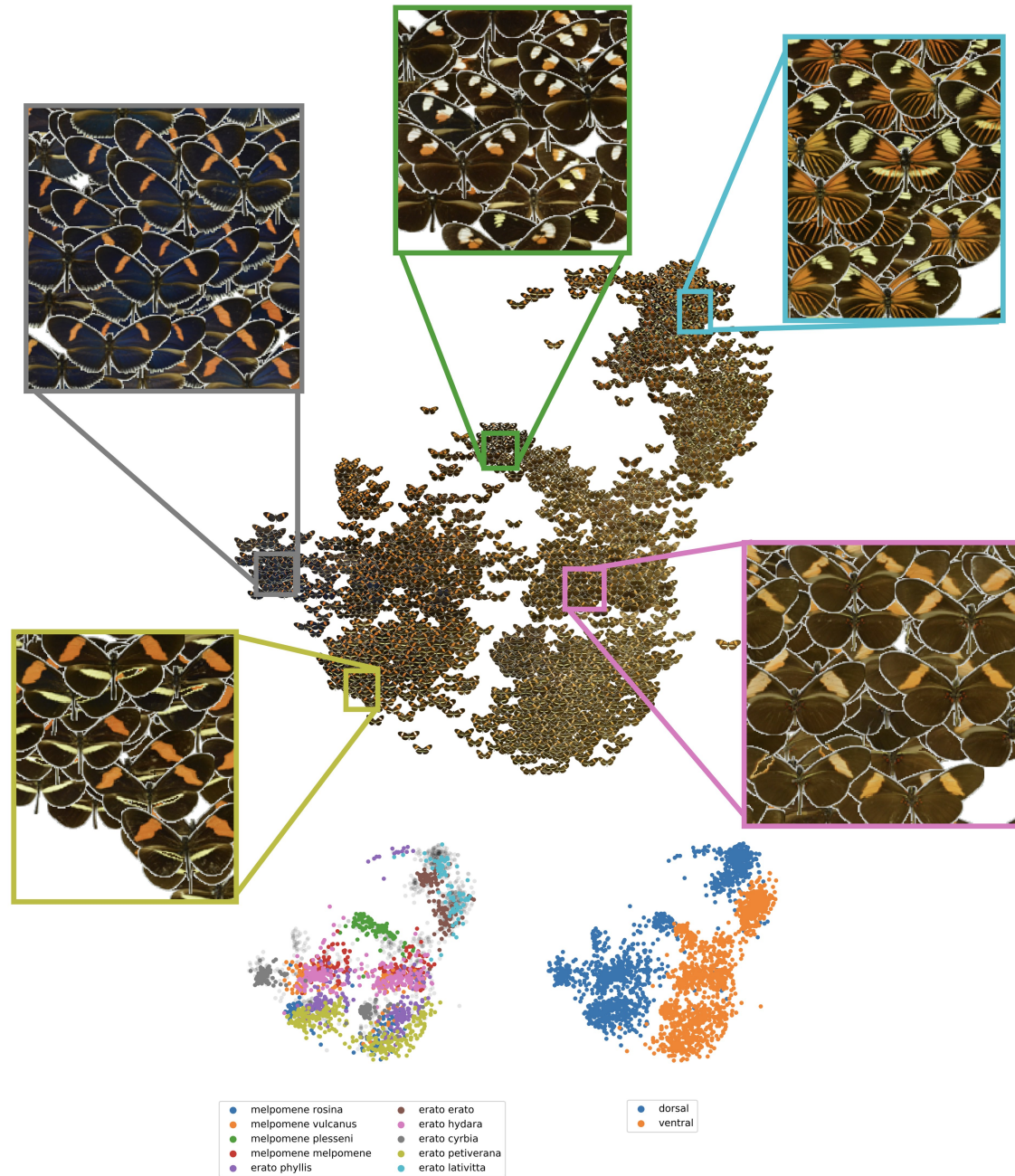


Figure S12. Embedding butterfly images. Butterfly (*Heliconius* spp.) images from Cuthill et al. (2019) embedded in two dimensions using convolutional VAE-SNE. Insets show example regions of perceptually similar subspecies (top). Scatter plots (bottom) show labels for the 10 most common subspecies in the dataset (bottom-left) and the image viewpoint relative to the specimen's dorso-ventral body axis (bottom-right).

Figure Video S1. Video segments labeled with VAE-SNE. Randomly selected video segments ($1/2\times$ speed) labeled with VAE-SNE illustrating the temporal dynamics of movements through the behavioral space and transitions between high-level clusters within the distribution. **a**, <https://youtu.be/JlbSdKzvLfk>; **b**, https://youtu.be/uWScG_UuzRQ; **c**, https://youtu.be/T8e_JSoCwMA

Figure Video S2. Samples from the locomotion cluster. Randomly sampled videos ($1/3\times$ speed) from the locomotion cluster showing: **a**, slow walking (<https://youtu.be/hB3JIRF2JGQ>); **b**, medium walking (<https://youtu.be/kNHGJypOGhs>); and **c**, fast walking (<https://youtu.be/A2sLtgYhHGc>). Red lines show the posture tracking data for all 32 keypoints.

Figure Video S3. Samples from the anterior grooming cluster. Randomly sampled videos ($1/3\times$ speed) from one of the anterior grooming clusters (<https://youtu.be/0MT3lb2bJro>). Red lines show the posture tracking data for all 32 keypoints.

Figure Video S4. Samples from the posterior grooming cluster. Randomly sampled videos ($1/3\times$ speed) from the posterior grooming cluster showing: **a**, bilateral hindleg grooming (https://youtu.be/O_Tyf4pEQMo); **b**, right hindleg grooming (<https://youtu.be/VTIwZp6d6b4>); **c**, left midleg grooming (<https://youtu.be/0vJvAINbfjw>). Red lines show the posture tracking data for all 32 keypoints.

Figure Video S5. Samples from the wing movements cluster. Randomly sampled videos ($1/3\times$ speed) from the wing movements cluster showing: **a**, wing extensions (<https://youtu.be/IE31SeJ7ehY>); and **b**, wing flicks (<https://youtu.be/nsgnFbrk090>). Red lines show the posture tracking data for all 32 keypoints.

Figure Video S6. Samples from the small/slow leg movements cluster. Randomly sampled videos ($1/3\times$ speed) from the small/slow leg movement cluster showing: **a**, small leg movements (<https://youtu.be/ARkH1uvPBnQ>); **b**, slow leg movements (<https://youtu.be/hwL7ovNjbBQ>); **c**, small left midleg movements (<https://youtu.be/o8vxtgwzx9Q>). Red lines show the posture tracking data for all 32 keypoints.

Figure Video S7. Samples from the idle cluster. Randomly sampled videos ($1/3\times$ speed) from the idle cluster (https://youtu.be/0wbdqmuCe_g). Red lines show the posture tracking data for all 32 keypoints.

Figure Video S8. Spherical embedding of the posture dynamics dataset. Rotating view of the posture dynamics dataset (<https://youtu.be/QcDUIQUOvdo>) from Berman et al. (2014, 2016); Pereira et al. (2019) embedded on a 3-D sphere using von Mises-Fisher VAE-SNE. Colors are the same as in Fig. 2 (total amplitude).

Figure Video S9. Spherical embedding of the single-cell RNA-seq dataset. Rotating view of the single-cell RNA-seq dataset (<https://youtu.be/jyIWB6-qye0>) from La Manno et al. (2018) embedded on a 3-D sphere using von Mises-Fisher VAE-SNE. Colors are the same as in Fig. 2 (cell type).

867 **A Variational autoencoders and the evidence lower bound**

868 **A.1 VAEs as approximate Bayesian inference**

869 As is common to most dimensionality reduction algorithms, we seek to model a high-dimensional data
870 distribution $p(\mathbf{x})$ using a low dimensional latent distribution $p(\mathbf{z})$. Variational autoencoders (VAEs) are
871 one such model that combines both modeling and inference by defining a joint distribution between a
872 latent variable \mathbf{z} and observed samples \mathbf{x} . We can accomplish this using a generative model that maps
873 samples from the low-dimensional latent distribution to the high-dimensional data distribution using a
874 set of shared parameters θ , which can take the form of a deep neural network model $p_{\theta}(\mathbf{x}|\mathbf{z}) = \text{DNN}_{\theta}(\mathbf{z})$
875 with some prior over latent distribution $p_{\theta}(\mathbf{z})$. We then wish to find the model parameters θ that
876 maximize the joint likelihood, which can be written as:

$$\arg \max_{\theta} p_{\theta}(\mathbf{x}, \mathbf{z}) = \arg \max_{\theta} p_{\theta}(\mathbf{x}|\mathbf{z})p_{\theta}(\mathbf{z}). \quad (10)$$

877 Although, to compute the low-dimensional distribution for the data, we then need to derive the latent
878 posterior for the model $p_{\theta}(\mathbf{z}|\mathbf{x})$. This can be derived from the likelihood using Bayes' rule:

$$p_{\theta}(\mathbf{z}|\mathbf{x}) = \frac{p_{\theta}(\mathbf{x}|\mathbf{z})p_{\theta}(\mathbf{z})}{p_{\theta}(\mathbf{x})}. \quad (11)$$

879 However, computing the integral in Eq. 11 $p_{\theta}(\mathbf{x}) = \int p_{\theta}(\mathbf{x}|\mathbf{z})p_{\theta}(\mathbf{z}) d\mathbf{z}$ is not tractable in practice.
880 Therefore, we require a way to approximate this latent posterior distribution, which is the exact problem
881 for which VAEs provide a tractable solution.

882 Like other VAE models (Kingma and Welling, 2013; Kingma et al., 2014; Burda et al., 2015;
883 Dilokthanakul et al., 2016; Ding et al., 2018; Dieng et al., 2019a), VAE-SNE performs dimensionality
884 reduction by nonlinearly mapping observed high-dimensional data vectors \mathbf{x} to a low-dimensional
885 embedding \mathbf{z} using a deep neural network (DNN) as an encoder function $\text{DNN}_{\phi} : \mathbf{x} \rightarrow \mathbf{z}$ (Eq. 12e) with
886 the goal of learning an approximate posterior over the latent distribution $q_{\phi}(\mathbf{z}|\mathbf{x})$ (Eq. 12d), where the
887 parameters of the approximate posterior are learned as a function of the data (Eq. 12e) and the encoder
888 parameters ϕ are then shared across observed samples – known as *amortization*. The model then
889 maps latent vectors sampled from the low-dimensional embedding (Eq. 12c) to reconstruct the original
890 high-dimensional space $\text{DNN}_{\theta} : \mathbf{z} \rightarrow \tilde{\mathbf{x}}$ (Eq. 12a) using a generative decoder function we defined earlier
891 (rewritten in Eq. 12b). More precisely:

$$\tilde{\mathbf{x}} \sim p_{\theta}(\mathbf{x}|\mathbf{z}) \quad (12a)$$

$$p_{\theta}(\mathbf{x}|\mathbf{z}) = \mathcal{L}(\mathbf{x}|\text{DNN}_{\theta}(\mathbf{z})) \quad (12b)$$

$$\mathbf{z} \sim q_{\phi}(\mathbf{z}|\mathbf{x}) \quad (12c)$$

$$q_{\phi}(\mathbf{z}|\mathbf{x}) = \mathcal{N}(\mathbf{z}|\boldsymbol{\mu}, \text{diag}(\boldsymbol{\sigma}^2)) \quad (12d)$$

$$(\boldsymbol{\mu}, \log \boldsymbol{\sigma}^2) = \text{DNN}_{\phi}(\mathbf{x}) \quad (12e)$$

892 where $\mathcal{L}(\mathbf{x}|\cdot)$ is a user-selected likelihood function parameterized by the decoder function $\text{DNN}_{\theta}(\mathbf{z})$, and
893 $\mathcal{N}(\cdot|\boldsymbol{\mu}, \text{diag}(\boldsymbol{\sigma}^2))$ is a multivariate Gaussian whose parameters $\boldsymbol{\mu}$ and $\boldsymbol{\sigma}^2$ are a specified by the encoder
894 function $\text{DNN}_{\phi}(\mathbf{x})$.

895 **A.2 Deriving the evidence lower bound**

896 After defining the generative model, we then wish to optimize the parameters of the encoder ϕ and
897 decoder θ – given a set of observed samples from a data distribution $\mathbf{x} \sim p(\mathbf{x})$ – so that the
898 approximate posterior distribution $q_{\phi}(\mathbf{z}|\mathbf{x})$ matches closely with the true latent posterior from the
899 generative decoder, or $q_{\phi}(\mathbf{z}|\mathbf{x}) \approx p_{\theta}(\mathbf{z}|\mathbf{x})$. In other words, we wish to minimize the divergence between
900 the two distributions, or:

$$\arg \min_{\theta, \phi} \mathbb{KL}[q_{\phi}(\mathbf{z}|\mathbf{x})||p_{\theta}(\mathbf{z}|\mathbf{x})] = \arg \min_{\theta, \phi} \int q_{\phi}(\mathbf{z}|\mathbf{x}) \log \frac{q_{\phi}(\mathbf{z}|\mathbf{x})}{p_{\theta}(\mathbf{z}|\mathbf{x})} d\mathbf{z}. \quad (13)$$

901 However, as we have already established, computing the true posterior is intractable, so researchers
 902 have derived a lower bound known as the evidence lower bound, or ELBO (Kingma and Welling, 2013),
 903 to approximate this objective. The ELBO can be derived directly from Eq.13 (Adams, 2020), which is
 904 written as:

$$\mathbb{KL}[q_{\phi}(\mathbf{z}|\mathbf{x})||p_{\theta}(\mathbf{z}|\mathbf{x})] = \int q_{\phi}(\mathbf{z}|\mathbf{x}) \log \frac{q_{\phi}(\mathbf{z}|\mathbf{x})}{p_{\theta}(\mathbf{z}|\mathbf{x})} d\mathbf{z} \quad (14a)$$

$$= \log p_{\theta}(\mathbf{x}) + \int q_{\phi}(\mathbf{z}|\mathbf{x}) \log \frac{q_{\phi}(\mathbf{z}|\mathbf{x})}{p_{\theta}(\mathbf{z}|\mathbf{x})} d\mathbf{z} - \log p_{\theta}(\mathbf{x}) \quad (14b)$$

$$= \log p_{\theta}(\mathbf{x}) + \int q_{\phi}(\mathbf{z}|\mathbf{x}) \log \frac{q_{\phi}(\mathbf{z}|\mathbf{x})}{p_{\theta}(\mathbf{z}|\mathbf{x})} d\mathbf{z} - \int \log q_{\phi}(\mathbf{z}|\mathbf{x}) p_{\theta}(\mathbf{x}) d\mathbf{z} \quad (14c)$$

$$= \log p_{\theta}(\mathbf{x}) + \int q_{\phi}(\mathbf{z}|\mathbf{x}) \log \frac{q_{\phi}(\mathbf{z}|\mathbf{x})}{p_{\theta}(\mathbf{z}|\mathbf{x}) p_{\theta}(\mathbf{x})} d\mathbf{z} \quad (14d)$$

$$= \log p_{\theta}(\mathbf{x}) - \mathbb{E}_{q_{\phi}(\mathbf{z}|\mathbf{x})} \left[\log \frac{p_{\theta}(\mathbf{x}, \mathbf{z})}{q_{\phi}(\mathbf{z}|\mathbf{x})} \right] \quad (14e)$$

$$= \log p_{\theta}(\mathbf{x}) - \text{ELBO}(\theta, \phi). \quad (14f)$$

905 Because the Kullback-Leibler divergence is strictly non-negative, the ELBO is then a lower bound on the
 906 log marginal likelihood. However, The ELBO can also be derived by applying Jensen's inequality, as is
 907 more common in the literature (Kingma and Welling, 2013), to directly calculate a lower bound on the log
 908 marginal likelihood, or:

$$\log p_{\theta}(\mathbf{x}) = \log \int p_{\theta}(\mathbf{x}, \mathbf{z}) d\mathbf{z} \quad (15a)$$

$$= \log \int p_{\theta}(\mathbf{x}, \mathbf{z}) \frac{q_{\phi}(\mathbf{z}|\mathbf{x})}{q_{\phi}(\mathbf{z}|\mathbf{x})} d\mathbf{z} \quad (15b)$$

$$= \log \mathbb{E}_{q_{\phi}(\mathbf{z}|\mathbf{x})} \left[\frac{p_{\theta}(\mathbf{x}, \mathbf{z})}{q_{\phi}(\mathbf{z}|\mathbf{x})} \right] \quad (15c)$$

$$\geq \mathbb{E}_{q_{\phi}(\mathbf{z}|\mathbf{x})} \left[\log \frac{p_{\theta}(\mathbf{x}, \mathbf{z})}{q_{\phi}(\mathbf{z}|\mathbf{x})} \right] = \text{ELBO}(\theta, \phi). \quad (15d)$$

909 To learn the latent distribution given the model and the data, the ELBO is then maximized to
 910 optimize the model parameters. Here we write this as a minimization of the negative ELBO, which can
 911 be further decomposed into separate terms for the log-likelihood and the divergence between the
 912 approximate posterior and the prior over the latent distribution, or:

$$\arg \min_{\theta, \phi} -\text{ELBO}(\theta, \phi) = \arg \min_{\theta, \phi} \mathbb{E}_{q_{\phi}(\mathbf{z}|\mathbf{x})} \left[\log \frac{q_{\phi}(\mathbf{z}|\mathbf{x})}{p_{\theta}(\mathbf{x}, \mathbf{z})} \right] \quad (16a)$$

$$= \arg \min_{\theta, \phi} \mathbb{E}_{q_{\phi}(\mathbf{z}|\mathbf{x})} \left[\log \frac{q_{\phi}(\mathbf{z}|\mathbf{x})}{p_{\theta}(\mathbf{z}) p_{\theta}(\mathbf{x}|\mathbf{z})} \right] \quad (16b)$$

$$= \arg \min_{\theta, \phi} -\mathbb{E}_{q_{\phi}(\mathbf{z}|\mathbf{x})} [\log p_{\theta}(\mathbf{x}|\mathbf{z})] + \mathbb{E}_{q_{\phi}(\mathbf{z}|\mathbf{x})} \left[\log \frac{q_{\phi}(\mathbf{z}|\mathbf{x})}{p_{\theta}(\mathbf{z})} \right] \quad (16c)$$

$$= \arg \min_{\theta, \phi} -\underbrace{\mathbb{E}_{q_{\phi}(\mathbf{z}|\mathbf{x})} [\log p_{\theta}(\mathbf{x}|\mathbf{z})]}_{\text{likelihood}} + \underbrace{\mathbb{E}_{q_{\phi}(\mathbf{z}|\mathbf{x})} \left[\log \frac{q_{\phi}(\mathbf{z}|\mathbf{x})}{p_{\theta}(\mathbf{z})} \right]}_{\text{divergence}}. \quad (16d)$$

913 The derivation of the ELBO has also been discussed at length elsewhere (e.g., Kingma and Welling
914 2013; Kingma et al. 2014; Burda et al. 2015; Alemi et al. 2016; Dilokthanakul et al. 2016; Alemi et al. 2017;
915 Ding et al. 2018; also see Kingma and Welling 2019 for a comprehensive introduction).

916 **A.3 Importance-weighted ELBO**

917 While we use only a single Monte Carlo sample from the approximate posterior per training batch, we
918 also include a hyperparameter for multiple samples per training batch using the importance-weighted
919 ELBO from Burda et al. (2015), which modifies how the expectation in Eq. 16c is calculated to produce a
920 tighter bound on the loss by implicitly increasing the complexity of the posterior (Cremer et al., 2017).
921 However, we did not see any obvious performance improvements when using the importance-weighted
922 objective, and increasing the number of Monte Carlo samples per batch also increases training time.
923 The general utility of calculating a tighter bound is also unclear (Rainforth et al., 2018) but this may be
924 related to the generalization ability of the model. We leave further exploration of this hyperparameter for
925 future work.

926 **B Stochastic neighbor regularization**

927 For computing pairwise similarities, we largely follow Hinton and Roweis (2003) and van der Maaten and
928 Hinton (2008) by modeling local neighborhoods as the probability of transitioning from a landmark point
929 to its nearby neighbors when performing a random walk initialized from the landmark. By modeling local
930 neighborhoods as probability distributions and then minimizing the divergence between the
931 neighborhood distributions in high- and low-dimensional space, we preserve more local structure within
932 the low-dimensional embedding than a standard VAE (Ding et al., 2018).

933 **High-dimensional transition probabilities** To accomplish this, pairwise transition probabilities in
934 high-dimensional space $t(\mathbf{x}_j|\mathbf{x}_i)$ are modelled by applying a Gaussian kernel to convert the pairwise
935 distances between data points $d(\mathbf{x}_i, \mathbf{x}_j)$ into conditional probabilities – with self transitions set to
936 $t(\mathbf{x}_i|\mathbf{x}_i) = 0$. While Ding et al. (2018) use these asymmetric conditional probabilities $t(\mathbf{x}_j|\mathbf{x}_i)$ directly for
937 the high-dimensional similarities, van der Maaten and Hinton (2008) show that symmetrizing the
938 pairwise similarities so that $p(\mathbf{x}_j|\mathbf{x}_i) = p(\mathbf{x}_i|\mathbf{x}_j)$ reduces susceptibility to outliers, which can become
939 ill-determined in the low-dimensional embedding with an asymmetric kernel. Therefore, we use the
940 symmetrized conditional probabilities, which are computed as:

$$p(\mathbf{x}_j|\mathbf{x}_i) = \frac{t(\mathbf{x}_j|\mathbf{x}_i) + t(\mathbf{x}_i|\mathbf{x}_j)}{\sum_n t(\mathbf{x}_n|\mathbf{x}_i) + t(\mathbf{x}_i|\mathbf{x}_n)} \quad (17a)$$

$$t(\mathbf{x}_j|\mathbf{x}_i) = \frac{\mathcal{N}(\mathbf{x}_j|\mathbf{x}_i, \zeta_i^2)}{\sum_n \mathcal{N}(\mathbf{x}_n|\mathbf{x}_i, \zeta_i^2)} = \frac{\exp(-d(\mathbf{x}_i, \mathbf{x}_j)^2/2\zeta_i^2)}{\sum_n \exp(-d(\mathbf{x}_i, \mathbf{x}_n)^2/2\zeta_i^2)}, \quad (17b)$$

941 for $n = 1, \dots, N$ and $n \neq i$, where $d(\cdot, \cdot)$ is a user-selected distance metric, such as the Euclidean
942 distance. The landmark data point \mathbf{x}_i can then be considered the mean, and ζ_i^2 is the variance of the
943 Gaussian kernel describing the local neighborhood around \mathbf{x}_i – thereby assigning more probability
944 mass to nearby neighbors. The variance ζ_i^2 is selected for each data point via binary search such that
945 $2^{H_i} \approx P$, where P is the desired perplexity (a user-defined hyperparameter), 2^{H_i} is the perplexity of the
946 kernel for the i th data point, which approximately corresponds to the number of nearest neighbors
947 considered by the kernel, and H_i is the Shannon entropy in bits, or:

$$H_i = \sum_j t(\mathbf{x}_j|\mathbf{x}_i) \log_2 t(\mathbf{x}_j|\mathbf{x}_i). \quad (18)$$

948 **Low-dimensional transition probabilities** The low-dimensional similarities $q_\phi(\mathbf{z}_j|\mathbf{z}_i)$ are then
949 calculated according to Hinton and Roweis (2003) and van der Maaten and Hinton (2008) using a kernel
950 function $w_\phi(\mathbf{z}_j|\mathbf{z}_i)$ to convert pairwise distances into conditional probabilities:

$$q_\phi(\mathbf{z}_j|\mathbf{z}_i) = \frac{w_\phi(\mathbf{z}_j|\mathbf{z}_i)}{\sum_n w_\phi(\mathbf{z}_n|\mathbf{z}_i)}. \quad (19)$$

951 As in high-dimensional space, self transitions are set to $q_\phi(\mathbf{z}_i|\mathbf{z}_i) = 0$. Here we test two kernel functions
952 for preserving Euclidean similarities.

953 **t-SNE kernel** First is the heavy-tailed Student's t -distributed kernel used for the t-SNE algorithm
954 (van der Maaten and Hinton, 2008) with the log probability function written as:

$$\log w_\phi(\mathbf{z}_j|\mathbf{z}_i) = \log \mathcal{T}(\mathbf{z}_j|\mathbf{z}_i, \nu_i, \tau_i) = -\left(\frac{\nu_i + 1}{2}\right) \log \left(1 + \frac{\|\mathbf{z}_i - \mathbf{z}_j\|^2}{\tau_i \nu_i}\right) - Z_i \quad (20a)$$

$$Z_i = \log \tau_i + \frac{\log(\nu_i \pi)}{2} + \Gamma\left(\frac{\nu_i}{2}\right) + \Gamma\left(\frac{\nu_i + 1}{2}\right), \quad (20b)$$

955 where τ_i is the scale, ν_i is the degrees of freedom, which varies the heavy-tails of the kernel, and $\Gamma(\cdot)$ is
956 the gamma function. We write this as a log probability to more clearly show the relationship with the
957 similarity loss term derived later in this section (Eq. 23c). The Student's t -distribution is used primarily to
958 alleviate the "crowding problem" (van der Maaten and Hinton, 2008) that can occur with other nonlinear
959 embedding algorithms, including the original SNE algorithm (Hinton and Roweis, 2003), where points are
960 too densely packed in the low-dimensional space and moderately distant points are "crushed" together
961 as an artifact of the embedding algorithm.

962 **SNE kernel** Secondly, we test a Gaussian kernel – the kernel used for the original SNE algorithm
963 (Hinton and Roweis, 2003; van der Maaten and Hinton, 2008) – with the log probability function:

$$\log w_\phi(\mathbf{z}_j|\mathbf{z}_i) = \log \mathcal{N}(\mathbf{z}_j|\mathbf{z}_i, \eta_i^2) = -\frac{\|\mathbf{z}_i - \mathbf{z}_j\|^2}{2\eta_i^2} + Z_i \quad (21a)$$

$$Z_i = \log \eta_i + \log \sqrt{2\pi}, \quad (21b)$$

964 where η_i^2 is the variance.

965 **Setting the kernel parameters** The kernel parameters for the low-dimensional similarities are typically
966 set to a constant value, such as $\tau_i = \nu_i = \eta_i = 1$ (van der Maaten and Hinton, 2008), or are scaled
967 linearly with the dimensionality of the latent embedding (van der Maaten, 2009), but we also test
968 similarity kernels where these parameters are learned for each data point, parameterized by the encoder
969 $\text{DNN}_\phi(\mathbf{x})$ – an idea proposed by van der Maaten (2009). When the kernel parameters are constant
970 across all data points, the log normalization terms (Eqs. 20b, 21b) used for calculating the log
971 probabilities can be omitted as an additive constant that has no effect on the calculations after
972 normalization. However, this term is potentially important for optimization when learning these
973 parameters as a function of each data point, so we include it in our calculations.

974 **Reinterpreting the similarity loss term** To maximize numerical stability when optimizing the similarity
975 term, we substitute the cross-entropy between the high-dimensional and low-dimensional similarities

976 $H[p(\mathbf{x}_j|\mathbf{x}_i), q_\phi(\mathbf{z}_j|\mathbf{z}_i)]$, which is proportional to the Kullback-Leibler divergence and, after dropping the
 977 expectation, can be derived as follows:

$$\sum_j \text{SNE}_{j|i}(\mathbf{x}_i, \mathbf{x}_j, \phi) = \sum_j \text{KL}[p(\mathbf{x}_j|\mathbf{x}_i) || q_\phi(\mathbf{z}_j|\mathbf{z}_i)] \quad (22a)$$

$$= \sum_j p(\mathbf{x}_j|\mathbf{x}_i) \log \frac{p(\mathbf{x}_j|\mathbf{x}_i)}{q_\phi(\mathbf{z}_j|\mathbf{z}_i)} \quad (22b)$$

$$= \underbrace{\sum_j p(\mathbf{x}_j|\mathbf{x}_i) \log p(\mathbf{x}_j|\mathbf{x}_i)}_{\text{-entropy}} - \underbrace{\sum_j p(\mathbf{x}_j|\mathbf{x}_i) \log q_\phi(\mathbf{z}_j|\mathbf{z}_i)}_{\text{cross entropy}} \quad (22c)$$

$$= \text{constant} - \sum_j p(\mathbf{x}_j|\mathbf{x}_i) \log q_\phi(\mathbf{z}_j|\mathbf{z}_i) \quad (22d)$$

$$\propto - \sum_j p(\mathbf{x}_j|\mathbf{x}_i) \log q_\phi(\mathbf{z}_j|\mathbf{z}_i) = \sum_j H[p(\mathbf{x}_j|\mathbf{x}_i), q_\phi(\mathbf{z}_j|\mathbf{z}_i)]. \quad (22e)$$

978 Consequently, the Kullback-Leibler divergence for the similarity term can be reinterpreted as the
 979 cross-entropy between the pairwise similarities up to an additive constant (the negative entropy of the
 980 high-dimensional similarities), which can be omitted for the purposes of optimization. To further
 981 improve numerical stability for this computation, the cross-entropy is decomposed into attractive and
 982 repulsive forces using the unnormalized similarities (following Ding et al. 2018; Kobak and Berens 2019),
 983 which is written as:

$$- \sum_j p(\mathbf{x}_j|\mathbf{x}_i) \log q_\phi(\mathbf{z}_j|\mathbf{z}_i) = - \sum_j p(\mathbf{x}_j|\mathbf{x}_i) \log \frac{w_\phi(\mathbf{z}_j|\mathbf{z}_i)}{\sum_n w_\phi(\mathbf{z}_n|\mathbf{z}_i)} \quad (23a)$$

$$= - \sum_j p(\mathbf{x}_j|\mathbf{x}_i) \log w_\phi(\mathbf{z}_j|\mathbf{z}_i) + \sum_j p(\mathbf{x}_j|\mathbf{x}_i) \log \sum_j w_\phi(\mathbf{z}_j|\mathbf{z}_i) \quad (23b)$$

$$= \underbrace{- \sum_j p(\mathbf{x}_j|\mathbf{x}_i) \log w_\phi(\mathbf{z}_j|\mathbf{z}_i)}_{\text{attract}} + \underbrace{\log \sum_j w_\phi(\mathbf{z}_j|\mathbf{z}_i)}_{\text{repel}}. \quad (23c)$$

984 This may also help to clarify why we wrote the low-dimensional kernels as log-probability functions in
 985 Eqs. 20a, 21a.

986 C Extensions of VAE-SNE

987 C.1 Spherical embeddings with a von Mises-Fisher kernel

988 In addition to embeddings with Euclidean geometry, we introduce a version of VAE-SNE that uses polar
 989 geometry and embeds high-dimensional data on the surface of a 3D unit sphere. We calculate the
 990 high-dimensional similarities according to Appendix B, but we alter the calculations for the transition
 991 probabilities by using the cosine similarity for the high-dimensional pairwise metric. After normalization,
 992 this is equivalent to using a (hyper)spherical von Mises-Fisher distribution as the similarity kernel, or:

$$t(\mathbf{x}_j|\mathbf{x}_i) = \frac{\mathcal{F}(\mathbf{x}_j|\mathbf{x}_i, \kappa_i)}{\sum_n \mathcal{F}(\mathbf{x}_n|\mathbf{x}_i, \kappa_i)} = \frac{\exp(\hat{\mathbf{x}}_i \cdot \hat{\mathbf{x}}_j^T \kappa_i)}{\sum_n \exp(\hat{\mathbf{x}}_i \cdot \hat{\mathbf{x}}_n^T \kappa_i)}, \quad (24)$$

993 where $\hat{\mathbf{x}}_i = \mathbf{x}_i / \|\mathbf{x}_i\|^2$ and κ_i is the concentration parameter (the inverse variance $\kappa_i = \varsigma_i^{-2}$), which is
 994 selected using binary search to match the perplexity to a desired value (see Appendix B for details). We

995 then calculate the low-dimensional similarities using a 3D von Mises-Fisher kernel to create a spherical
996 embedding:

$$\log w_{\phi}(\mathbf{z}_j|\mathbf{z}_i) = \log \mathcal{F}(\mathbf{z}_j|\mathbf{z}_i, \rho_i) = \hat{\mathbf{z}}_i \cdot \hat{\mathbf{z}}_j^T \rho_i + Z_i \quad (25a)$$

$$Z_i = \log \rho_i - \log \sinh \rho_i - \log 4\pi \quad (25b)$$

997 where $\hat{\mathbf{z}}_i = \mathbf{z}_i/\|\mathbf{z}_i\|^2$ and ρ_i is the concentration parameter (inverse variance). The log normalization
998 term (Eq. 25b) can be omitted when ρ_i is set to a constant, but we include it for the purposes of
999 optimizing ρ_i as a function of each data point.

1000 The idea of using spherical embeddings for dimensionality reduction has been explored previously
1001 with the von Mises-Fisher stochastic neighbor embedding (VMF-SNE) algorithm (Wang and Wang, 2016)
1002 as well as more recent work by Ding and Regev (2019) who apply this type of embedding to visualize
1003 single-cell RNA-seq data. The UMAP algorithm (McInnes et al., 2018) has a similar option to embed data
1004 in polar coordinates, as well as other non-Euclidean spaces. VAEs with (hyper)spherical latent variables
1005 have also been explored extensively in the machine learning literature (Davidson et al. 2018; reviewed by
1006 Ding and Regev 2019). This type of spherical representation can be useful for data analysis, as
1007 high-dimensional vectors are often more accurately represented in polar coordinates. Similar to a
1008 heavy-tailed Student's t similarity kernel (van der Maaten and Hinton, 2008), a spherical von Mises-Fisher
1009 similarity kernel can also prevent "crowding" of the data toward the center of the latent coordinate
1010 system (Davidson et al., 2018; Ding and Regev, 2019), which is undesirable for visualizing data (van der
1011 Maaten and Hinton, 2008). To test this extension, we use von Mises-Fisher VAE-SNE to embed the
1012 posture dynamics dataset from Berman et al. (2014, 2016); Pereira et al. (2019) as well as the single-cell
1013 RNA-seq dataset from La Manno et al. (2018) and visualize the embeddings across the three dimensions
1014 of the unit sphere (Fig. S10; Video S8; Video S9). We find that the results are qualitatively similar to 2-D
1015 Euclidean embeddings of the same data (Fig. 2), but are instead embedded across a 3-D sphere. Despite
1016 not using a heavy-tailed similarity kernel (van der Maaten and Hinton, 2008) these spherical embeddings
1017 naturally do not exhibit any crowding problems (Davidson et al., 2018; Ding and Regev, 2019), which may
1018 make this a useful visualization tool for some scenarios.

1019 C.2 Convolutional VAE-SNE for image data

1020 We introduce a convolutional version of VAE-SNE for embedding image data from raw pixels. This
1021 version of VAE-SNE is modified by first applying a 2-D convolutional neural network CNN_{ϕ} – a
1022 SqueezeNet v1.1 (Iandola et al., 2016) pretrained on ImageNet (Deng et al., 2009) – to each image and
1023 then calculating the pairwise similarity using spatially-pooled feature maps from the CNN_{ϕ} output. The
1024 high-dimensional transition probabilities (Appendix B) are then calculated using a Gaussian kernel:

$$t(\mathbf{x}_j|\mathbf{x}_i) = \frac{\exp(-d(\hat{\mathbf{v}}_i, \hat{\mathbf{v}}_j)^2/2\zeta_i^2)}{\sum_n \exp(-d(\hat{\mathbf{v}}_i, \hat{\mathbf{v}}_n)^2/2\zeta_i^2)}, \quad (26)$$

1025 where $\hat{\mathbf{v}}_i$ is a vector of spatially-pooled feature maps from the CNN_{ϕ} output, or $\hat{\mathbf{v}}_i = \text{CNN}_{\phi}(\mathbf{x}_i)$. The
1026 approximate posterior is then calculated as a nonlinear function of the pooled feature maps
1027 $\text{DNN}_{\phi} : \hat{\mathbf{v}}_i \rightarrow \mathbf{z}_i$, which is written as $q_{\phi}(\mathbf{z}|\mathbf{x}_i) = \mathcal{N}(\mathbf{z}|\text{DNN}_{\phi}(\hat{\mathbf{v}}_i))$. For the decoder we use a feed-forward
1028 network $\text{DNN}_{\theta} : \mathbf{z}_i \rightarrow \tilde{\mathbf{v}}_i$ as before, where $\tilde{\mathbf{v}}_i$ is a reconstruction of the CNN_{ϕ} output $\hat{\mathbf{v}}_i$. We then apply
1029 mean squared error between the pooled feature maps and the reconstruction as the likelihood function
1030 for the distortion loss (Eq. 1b). A convolutional decoder could also be used to fully reconstruct the raw
1031 image pixels, but we found simply reconstructing the pooled feature maps to be effective for visualizing
1032 the distribution of images in two dimensions.

1033 To demonstrate the utility of convolutional VAE-SNE, we embed natural history image datasets of
1034 both shells (Zhang et al., 2019) and (*Heliconius spp.*) butterflies (Cuthill et al., 2019). We then visualize
1035 these embeddings to qualitatively assess performance of this VAE-SNE variant (Figs. S11, S12). We find

1036 that perceptually similar images are grouped together in the embedding based on complex sets of
1037 image features – rather than simple heuristics like color – and these groupings correspond to
1038 taxonomic relationships within the dataset, which were not explicitly included as part of the training set.
1039 This variant of VAE-SNE is functionally similar to using the perceptual distance (Johnson et al., 2016a;
1040 Wham et al., 2019) as a similarity metric and likelihood function except that the model can be trained
1041 end-to-end with small batches of images directly using raw pixels instead of first preprocessing images
1042 to produce feature activations. These results demonstrate that VAE-SNE can be used to analyze very
1043 large image datasets, by loading images in small batches, and can also be extended to images with
1044 variable resolution, by integrating across feature map outputs from the CNN to remove the spatial
1045 dimension – both of which are typically not possible with other dimension reduction algorithms.

References

- R. P. Adams. The elbo without jensen, kullback, or leibler. <https://lips.cs.princeton.edu/the-elbo-without-jensen-or-kl/>, June 2020.
- M. B. Ahrens, J. M. Li, M. B. Orger, D. N. Robson, A. F. Schier, F. Engert, and R. Portugues. Brain-wide neuronal dynamics during motor adaptation in zebrafish. *Nature*, 485(7399):471, 2012.
- M. B. Ahrens, M. B. Orger, D. N. Robson, J. M. Li, and P. J. Keller. Whole-brain functional imaging at cellular resolution using light-sheet microscopy. *Nature methods*, 10(5):413, 2013.
- A. A. Alemi, I. Fischer, J. V. Dillon, and K. Murphy. Deep variational information bottleneck. *arXiv preprint arXiv:1612.00410*, 2016.
- A. A. Alemi, B. Poole, I. Fischer, J. V. Dillon, R. A. Saurous, and K. Murphy. Fixing a broken elbo. *arXiv preprint arXiv:1711.00464*, 2017.
- D. J. Anderson and P. Perona. Toward a science of computational ethology. *Neuron*, 84(1):18–31, 2014.
- P. C. Bala, B. R. Eisenreich, S. B. M. Yoo, B. Y. Hayden, H. S. Park, and J. Zimmermann. Openmonkeystudio: automated markerless pose estimation in freely moving macaques. *bioRxiv*, 2020.
- D. E. Bath, J. R. Stowers, D. Hörmann, A. Poehlmann, B. J. Dickson, and A. D. Straw. Flymad: rapid thermogenetic control of neuronal activity in freely walking drosophila. *Nature methods*, 11(7):756, 2014.
- E. Becht, L. McInnes, J. Healy, C.-A. Dutertre, I. W. Kwok, L. G. Ng, F. Ginhoux, and E. W. Newell. Dimensionality reduction for visualizing single-cell data using umap. *Nature biotechnology*, 37(1):38, 2019.
- G. J. Berman. Measuring behavior across scales. *BMC biology*, 16(1):23, 2018.
- G. J. Berman, D. M. Choi, W. Bialek, and J. W. Shaevitz. Mapping the stereotyped behaviour of freely moving fruit flies. *Journal of The Royal Society Interface*, 11(99):20140672, 2014.
- G. J. Berman, W. Bialek, and J. W. Shaevitz. Predictability and hierarchy in drosophila behavior. *Proceedings of the National Academy of Sciences*, 113(42):11943–11948, 2016.
- J. C. Billings, A. Medda, S. Shakil, X. Shen, A. Kashyap, S. Chen, A. Abbas, X. Zhang, M. Nezafati, W.-J. Pan, et al. Instantaneous brain dynamics mapped to a continuous state space. *Neuroimage*, 162: 344–352, 2017.
- B. M. Bolker, M. E. Brooks, C. J. Clark, S. W. Geange, J. R. Poulsen, M. H. H. Stevens, and J.-S. S. White. Generalized linear mixed models: a practical guide for ecology and evolution. *Trends in ecology & evolution*, 24(3):127–135, 2009.
- A. E. Brown and B. De Bivort. Ethology as a physical science. *Nature Physics*, page 1, 2018.
- A. E. Brown, E. I. Yemini, L. J. Grundy, T. Jucikas, and W. R. Schafer. A dictionary of behavioral motifs reveals clusters of genes affecting caenorhabditis elegans locomotion. *Proceedings of the National Academy of Sciences*, 110(2):791–796, 2013.
- L. Buitinck, G. Louppe, M. Blondel, F. Pedregosa, A. Mueller, O. Grisel, V. Niculae, P. Prettenhofer, A. Gramfort, J. Grobler, R. Layton, J. VanderPlas, A. Joly, B. Holt, and G. Varoquaux. API design for machine learning software: experiences from the scikit-learn project. In *ECML PKDD Workshop: Languages for Data Mining and Machine Learning*, pages 108–122, 2013.

- Y. Burda, R. Grosse, and R. Salakhutdinov. Importance weighted autoencoders. *arXiv preprint arXiv:1509.00519*, 2015.
- R. J. Campello, D. Moulavi, and J. Sander. Density-based clustering based on hierarchical density estimates. In *Pacific-Asia conference on knowledge discovery and data mining*, pages 160–172. Springer, 2013.
- J. Cande, S. Namiki, J. Qiu, W. Korff, G. M. Card, J. W. Shaevitz, D. L. Stern, and G. J. Berman. Optogenetic dissection of descending behavioral control in drosophila. *Elife*, 7:e34275, 2018.
- M. Chalk, O. Marre, and G. Tkacik. Relevant sparse codes with variational information bottleneck. In *Advances in Neural Information Processing Systems*, pages 1957–1965, 2016.
- C. Chambers, G. Kong, K. Wei, and K. Kording. Pose estimates from online videos show that side-by-side walkers synchronize movement under naturalistic conditions. *PloS one*, 14(6):e0217861, 2019.
- T. Chen, S. Kornblith, M. Norouzi, and G. Hinton. A simple framework for contrastive learning of visual representations. *arXiv preprint arXiv:2002.05709*, 2020.
- J.-T. Chien and C.-W. Hsu. Variational manifold learning for speaker recognition. In *2017 IEEE International Conference on Acoustics, Speech and Signal Processing (ICASSP)*, pages 4935–4939. IEEE, 2017.
- H. Cho, B. Berger, and J. Peng. Generalizable and scalable visualization of single-cell data using neural networks. *Cell systems*, 7(2):185–191, 2018.
- D.-A. Clevert, T. Unterthiner, and S. Hochreiter. Fast and accurate deep network learning by exponential linear units (elus). *arXiv preprint arXiv:1511.07289*, 2015.
- A. C. Costa, T. Ahamed, and G. J. Stephens. Adaptive, locally linear models of complex dynamics. *Proceedings of the National Academy of Sciences*, 116(5):1501–1510, 2019. ISSN 0027-8424. doi: 10.1073/pnas.1813476116. URL <https://www.pnas.org/content/116/5/1501>.
- C. Cremer, Q. Morris, and D. Duvenaud. Reinterpreting importance-weighted autoencoders. *arXiv preprint arXiv:1704.02916*, 2017.
- I. C. Cuthill, W. L. Allen, K. Arbuckle, B. Caspers, G. Chaplin, M. E. Hauber, G. E. Hill, N. G. Jablonski, C. D. Jiggins, A. Kelber, et al. The biology of color. *Science*, 357(6350):eaan0221, 2017.
- J. F. H. Cuthill, N. Guttenberg, S. Ledger, R. Crowther, and B. Huertas. Deep learning on butterfly phenotypes tests evolution’s oldest mathematical model. *Science advances*, 5(8):eaaw4967, 2019.
- S. R. Datta, D. J. Anderson, K. Branson, P. Perona, and A. Leifer. Computational neuroethology: a call to action. *Neuron*, 104(1):11–24, 2019.
- T. R. Davidson, L. Falorsi, N. De Cao, T. Kipf, and J. M. Tomczak. Hyperspherical variational auto-encoders. *arXiv preprint arXiv:1804.00891*, 2018.
- J. Deng, W. Dong, R. Socher, L.-J. Li, K. Li, and L. Fei-Fei. Imagenet: A large-scale hierarchical image database. In *2009 IEEE conference on computer vision and pattern recognition*, pages 248–255. IEEE, 2009.
- A. B. Dieng, Y. Kim, A. M. Rush, and D. M. Blei. Avoiding latent variable collapse with generative skip models. In *The 22nd International Conference on Artificial Intelligence and Statistics*, pages 2397–2405, 2019a.
- A. B. Dieng, F. J. Ruiz, D. M. Blei, and M. K. Titsias. Prescribed generative adversarial networks. *arXiv preprint arXiv:1910.04302*, 2019b.

- N. Dilokthanakul, P. A. Mediano, M. Garnelo, M. C. Lee, H. Salimbeni, K. Arulkumaran, and M. Shanahan. Deep unsupervised clustering with gaussian mixture variational autoencoders. *arXiv preprint arXiv:1611.02648*, 2016.
- J. Ding and A. Regev. Deep generative model embedding of single-cell rna-seq profiles on hyperspheres and hyperbolic spaces. *BioRxiv*, page 853457, 2019.
- J. Ding, A. Condon, and S. P. Shah. Interpretable dimensionality reduction of single cell transcriptome data with deep generative models. *Nature Communications*, 9(1):2002, 2018. doi: 10.1038/s41467-018-04368-5. URL <https://doi.org/10.1038/s41467-018-04368-5>.
- J. A. Doudna and E. Charpentier. The new frontier of genome engineering with crispr-cas9. *Science*, 346(6213):1258096, 2014.
- C. L. Ebbesen and R. C. Froemke. Automatic tracking of mouse social posture dynamics by 3d videography, deep learning and gpu-accelerated robust optimization. *bioRxiv*, 2020. doi: 10.1101/2020.05.21.109629. URL <https://www.biorxiv.org/content/early/2020/05/25/2020.05.21.109629>.
- B. D. Ezray, D. C. Wham, C. E. Hill, and H. M. Hines. Unsupervised machine learning reveals mimicry complexes in bumblebees occur along a perceptual continuum. *Proceedings of the Royal Society B*, 286(1910):20191501, 2019.
- Y. Fang and J. Wang. Selection of the number of clusters via the bootstrap method. *Computational Statistics & Data Analysis*, 56(3):468–477, 2012.
- S. Fogel, H. Averbuch-Elor, D. Cohen-Or, and J. Goldberger. Clustering-driven deep embedding with pairwise constraints. *IEEE computer graphics and applications*, 39(4):16–27, 2019.
- I. Goodfellow, J. Pouget-Abadie, M. Mirza, B. Xu, D. Warde-Farley, S. Ozair, A. Courville, and Y. Bengio. Generative adversarial nets. In *Advances in neural information processing systems*, pages 2672–2680, 2014.
- I. Goodfellow, Y. Bengio, and A. Courville. *Deep learning*. MIT press, 2016.
- J. M. Graving. behavellet: a wavelet transform for mapping behavior, Aug. 2019. URL <https://doi.org/10.5281/zenodo.3376742>.
- J. M. Graving, D. Chae, H. Naik, L. Li, B. Koger, B. R. Costelloe, and I. D. Couzin. Deepposekit, a software toolkit for fast and robust animal pose estimation using deep learning. *eLife*, 8:e47994, 2019.
- D. Grün, A. Lyubimova, L. Kester, K. Wiebrands, O. Basak, N. Sasaki, H. Clevers, and A. van Oudenaarden. Single-cell messenger rna sequencing reveals rare intestinal cell types. *Nature*, 525(7568):251, 2015.
- S. Günel, H. Rhodin, D. Morales, J. Campagnolo, P. Ramdya, and P. Fua. Deepfly3d, a deep learning-based approach for 3d limb and appendage tracking in tethered, adult drosophila. *eLife*, 8, 2019.
- X. Guo, L. Gao, X. Liu, and J. Yin. Improved deep embedded clustering with local structure preservation. In *IJCAI*, pages 1753–1759, 2017.
- D. Hafner, D. Tran, T. Lillicrap, A. Irpan, and J. Davidson. Reliable uncertainty estimates in deep neural networks using noise contrastive priors. 2018.
- I. Higgins, L. Matthey, A. Pal, C. Burgess, X. Glorot, M. Botvinick, S. Mohamed, and A. Lerchner. beta-vae: Learning basic visual concepts with a constrained variational framework. 2016.
- I. Higgins, L. Matthey, A. Pal, C. Burgess, X. Glorot, M. Botvinick, S. Mohamed, and A. Lerchner. beta-vae: Learning basic visual concepts with a constrained variational framework. *Iclr*, 2(5):6, 2017.

- G. E. Hinton and S. T. Roweis. Stochastic neighbor embedding. In *Advances in neural information processing systems*, pages 857–864, 2003.
- G. E. Hinton and R. R. Salakhutdinov. Reducing the dimensionality of data with neural networks. *science*, 313(5786):504–507, 2006.
- F. N. Iandola, S. Han, M. W. Moskewicz, K. Ashraf, W. J. Dally, and K. Keutzer. Squeezenet: Alexnet-level accuracy with 50x fewer parameters and 0.5 mb model size. *arXiv preprint arXiv:1602.07360*, 2016.
- D. J. Im, N. Verma, and K. Branson. Stochastic neighbor embedding under f-divergences. *arXiv preprint arXiv:1811.01247*, 2018.
- A. K. Jain, M. N. Murty, and P. J. Flynn. Data clustering: a review. *ACM computing surveys (CSUR)*, 31(3): 264–323, 1999.
- E. Jang, S. Gu, and B. Poole. Categorical reparameterization with gumbel-softmax. *arXiv preprint arXiv:1611.01144*, 2016.
- Z. Jiang, Y. Zheng, H. Tan, B. Tang, and H. Zhou. Variational deep embedding: An unsupervised and generative approach to clustering. *arXiv preprint arXiv:1611.05148*, 2016.
- J. Johnson, A. Alahi, and L. Fei-Fei. Perceptual losses for real-time style transfer and super-resolution. In *European conference on computer vision*, pages 694–711. Springer, 2016a.
- M. Johnson, D. K. Duvenaud, A. Wiltchko, R. P. Adams, and S. R. Datta. Composing graphical models with neural networks for structured representations and fast inference. In *Advances in neural information processing systems*, pages 2946–2954, 2016b.
- J. J. Jun, N. A. Steinmetz, J. H. Siegle, D. J. Denman, M. Bauza, B. Barbarits, A. K. Lee, C. A. Anastassiou, A. Andrei, Ç. Aydin, et al. Fully integrated silicon probes for high-density recording of neural activity. *Nature*, 551(7679):232, 2017.
- J. Kain, C. Stokes, Q. Gaudry, X. Song, J. Foley, R. Wilson, and B. De Bivort. Leg-tracking and automated behavioural classification in drosophila. *Nature communications*, 4:1910, 2013.
- B. Kang, D. G. García, J. Lijffijt, R. Santos-Rodríguez, and T. De Bie. Conditional t-sne: Complementary t-sne embeddings through factoring out prior information. *arXiv preprint arXiv:1905.10086*, 2019.
- P. Karashchuk, K. L. Rupp, E. S. Dickinson, E. Sanders, E. Azim, B. W. Brunton, and J. C. Tuthill. Anipose: a toolkit for robust markerless 3d pose estimation. *bioRxiv*, 2020.
- A. Kendall and Y. Gal. What uncertainties do we need in bayesian deep learning for computer vision? In *Advances in neural information processing systems*, pages 5574–5584, 2017.
- D. P. Kingma and J. Ba. Adam: A method for stochastic optimization. *arXiv preprint arXiv:1412.6980*, 2014.
- D. P. Kingma and M. Welling. Auto-encoding variational bayes. *arXiv preprint arXiv:1312.6114*, 2013.
- D. P. Kingma and M. Welling. An introduction to variational autoencoders. *arXiv preprint arXiv:1906.02691*, 2019.
- D. P. Kingma, S. Mohamed, D. J. Rezende, and M. Welling. Semi-supervised learning with deep generative models. In *Advances in neural information processing systems*, pages 3581–3589, 2014.
- D. P. Kingma, T. Salimans, R. Jozefowicz, X. Chen, I. Sutskever, and M. Welling. Improved variational inference with inverse autoregressive flow. In *Advances in neural information processing systems*, pages 4743–4751, 2016.

- G. Klambauer, T. Unterthiner, A. Mayr, and S. Hochreiter. Self-normalizing neural networks. In *Advances in neural information processing systems*, pages 971–980, 2017.
- J. M. Kleinberg. An impossibility theorem for clustering. In *Advances in neural information processing systems*, pages 463–470, 2003.
- U. Klibaite and J. W. Shaevitz. Interacting fruit flies synchronize behavior. *bioRxiv*, page 545483, 2019.
- U. Klibaite, G. J. Berman, J. Cande, D. L. Stern, and J. W. Shaevitz. An unsupervised method for quantifying the behavior of paired animals. *Physical biology*, 14(1):015006, 2017.
- D. Kobak and P. Berens. The art of using t-sne for single-cell transcriptomics. *Nature communications*, 10(1):1–14, 2019.
- D. Kobak and G. C. Linderman. Umap does not preserve global structure any better than t-sne when using the same initialization. *bioRxiv*, 2019.
- G. La Manno, R. Soldatov, A. Zeisel, E. Braun, H. Hochgerner, V. Petukhov, K. Lidschreiber, M. E. Kastrioti, P. Lönnerberg, A. Furlan, et al. Rna velocity of single cells. *Nature*, 560(7719):494–498, 2018.
- S. K. Lam, A. Pitrou, and S. Seibert. Numba: A llvm-based python jit compiler. In *Proceedings of the Second Workshop on the LLVM Compiler Infrastructure in HPC*, pages 1–6, 2015.
- A. B. L. Larsen, S. K. Sønderby, H. Larochelle, and O. Winther. Autoencoding beyond pixels using a learned similarity metric. In *International conference on machine learning*, pages 1558–1566, 2016.
- Y. LeCun, C. Cortes, and C. Burges. Mnist handwritten digit database. 2010.
- G. C. Linderman, M. Rachh, J. G. Hoskins, S. Steinerberger, and Y. Kluger. Efficient algorithms for t-distributed stochastic neighborhood embedding. *arXiv preprint arXiv:1712.09005*, 2017.
- G. C. Linderman, M. Rachh, J. G. Hoskins, S. Steinerberger, and Y. Kluger. Fast interpolation-based t-sne for improved visualization of single-cell rna-seq data. *Nature methods*, 16(3):243–245, 2019.
- K. Luxem, F. Fuhrmann, J. Kürsch, S. Remy, and P. Bauer. Identifying behavioral structure from deep variational embeddings of animal motion. *bioRxiv*, 2020.
- C. J. Maddison, A. Mnih, and Y. W. Teh. The concrete distribution: A continuous relaxation of discrete random variables. *arXiv preprint arXiv:1611.00712*, 2016.
- J. E. Markowitz, W. F. Gillis, C. C. Beron, S. Q. Neufeld, K. Robertson, N. D. Bhagat, R. E. Peterson, E. Peterson, M. Hyun, S. W. Linderman, et al. The striatum organizes 3d behavior via moment-to-moment action selection. *Cell*, 174(1):44–58, 2018.
- A. Mathis, P. Mamidanna, K. M. Cury, T. Abe, V. N. Murthy, M. W. Mathis, and M. Bethge. Deeplabcut: markerless pose estimation of user-defined body parts with deep learning. *Nature Neuroscience*, 2018. URL <https://www.nature.com/articles/s41593-018-0209-y>.
- A. F. McDaid, D. Greene, and N. Hurley. Normalized mutual information to evaluate overlapping community finding algorithms. *arXiv preprint arXiv:1110.2515*, 2011.
- L. McInnes, J. Healy, and S. Astels. hdbscan: Hierarchical density based clustering. *Journal of Open Source Software*, 2(11):205, 2017.
- L. McInnes, J. Healy, and J. Melville. Umap: Uniform manifold approximation and projection for dimension reduction. *arXiv preprint arXiv:1802.03426*, 2018.
- C. S. Mendes, I. Bartos, T. Akay, S. Márka, and R. S. Mann. Quantification of gait parameters in freely walking wild type and sensory deprived drosophila melanogaster. *elife*, 2:e00231, 2013.

- G. W. Milligan and M. C. Cooper. An examination of procedures for determining the number of clusters in a data set. *Psychometrika*, 50(2):159–179, 1985.
- C. E. Moody. topicsne: t-sne experiments in pytorch. <https://github.com/cemoody/topicsne>; archived at: <https://github.com/jgraving/topicsne>, March 2017.
- A. Narayan, B. Berger, and H. Cho. Density-preserving data visualization unveils dynamic patterns of single-cell transcriptomic variability. *bioRxiv*, 2020.
- T. Nath, A. Mathis, A. C. Chen, A. Patel, M. Bethge, and M. W. Mathis. Using deeplabcut for 3d markerless pose estimation across species and behaviors. *Nature protocols*, 14(7):2152–2176, 2019.
- A. v. d. Oord, S. Dieleman, H. Zen, K. Simonyan, O. Vinyals, A. Graves, N. Kalchbrenner, A. Senior, and K. Kavukcuoglu. Wavenet: A generative model for raw audio. *arXiv preprint arXiv:1609.03499*, 2016.
- C. Pandarinath, D. J. O’Shea, J. Collins, R. Jozefowicz, S. D. Stavisky, J. C. Kao, E. M. Trautmann, M. T. Kaufman, S. I. Ryu, L. R. Hochberg, et al. Inferring single-trial neural population dynamics using sequential auto-encoders. *Nature methods*, 15(10):805–815, 2018.
- G. Papamakarios, T. Pavlakou, and I. Murray. Masked autoregressive flow for density estimation. In *Advances in Neural Information Processing Systems*, pages 2338–2347, 2017.
- A. Paszke, S. Gross, F. Massa, A. Lerer, J. Bradbury, G. Chanan, T. Killeen, Z. Lin, N. Gimelshein, L. Antiga, et al. Pytorch: An imperative style, high-performance deep learning library. In *Advances in Neural Information Processing Systems*, pages 8024–8035, 2019.
- F. Pedregosa, G. Varoquaux, A. Gramfort, V. Michel, B. Thirion, O. Grisel, M. Blondel, P. Prettenhofer, R. Weiss, V. Dubourg, J. Vanderplas, A. Passos, D. Cournapeau, M. Brucher, M. Perrot, and E. Duchesnay. Scikit-learn: Machine learning in Python. *Journal of Machine Learning Research*, 12: 2825–2830, 2011.
- T. D. Pereira, D. E. Aldarondo, L. Willmore, M. Kislin, S. S.-H. Wang, M. Murthy, and J. W. Shaevitz. Fast animal pose estimation using deep neural networks. *Nature methods*, 16(1):117, 2019.
- N. Pezzotti, T. Höllt, B. Lelieveldt, E. Eisemann, and A. Vilanova. Hierarchical stochastic neighbor embedding. In *Computer Graphics Forum*, volume 35, pages 21–30. Wiley Online Library, 2016.
- D. T. Pham, S. S. Dimov, and C. D. Nguyen. Selection of k in k-means clustering. *Proceedings of the Institution of Mechanical Engineers, Part C: Journal of Mechanical Engineering Science*, 219(1): 103–119, 2005.
- P. G. Poličar, M. Stražar, and B. Zupan. Embedding to reference t-sne space addresses batch effects in single-cell classification. In *International Conference on Discovery Science*, pages 246–260. Springer, 2019.
- P. G. Poličar, M. Strazar, and B. Zupan. opentsne: a modular python library for t-sne dimensionality reduction and embedding. *BioRxiv*, page 731877, 2019.
- B. Poole, S. Ozair, A. v. d. Oord, A. A. Alemi, and G. Tucker. On variational bounds of mutual information. *arXiv preprint arXiv:1905.06922*, 2019.
- T. Rainforth, A. R. Kosiorek, T. A. Le, C. J. Maddison, M. Igl, F. Wood, and Y. W. Teh. Tighter variational bounds are not necessarily better. *arXiv preprint arXiv:1802.04537*, 2018.
- F. A. Ran, P. D. Hsu, J. Wright, V. Agarwala, D. A. Scott, and F. Zhang. Genome engineering using the crispr-cas9 system. *Nature protocols*, 8(11):2281, 2013.
- A. Razavi, A. van den Oord, and O. Vinyals. Generating diverse high-fidelity images with vq-vae-2. In *Advances in Neural Information Processing Systems*, pages 14866–14876, 2019.

- A. L. Rezaabad and S. Vishwanath. Learning representations by maximizing mutual information in variational autoencoder. *arXiv preprint arXiv:1912.13361*, 2019.
- D. J. Rezende and S. Mohamed. Variational inference with normalizing flows. *arXiv preprint arXiv:1505.05770*, 2015.
- D. J. Rezende, S. Mohamed, and D. Wierstra. Stochastic backpropagation and approximate inference in deep generative models. *arXiv preprint arXiv:1401.4082*, 2014.
- A. Roberts, J. Engel, C. Raffel, C. Hawthorne, and D. Eck. A hierarchical latent vector model for learning long-term structure in music. *arXiv preprint arXiv:1803.05428*, 2018.
- I. Robinson and E. Pierce-Hoffman. Tree-sne: Hierarchical clustering and visualization using t-sne. *arXiv preprint arXiv:2002.05687*, 2020.
- M. Rolinek, D. Zietlow, and G. Martius. Variational autoencoders pursue pca directions (by accident). In *Proceedings of the IEEE Conference on Computer Vision and Pattern Recognition*, pages 12406–12415, 2019.
- T. Sainburg, M. Thielk, and T. Q. Gentner. Latent space visualization, characterization, and generation of diverse vocal communication signals. *bioRxiv*, page 870311, 2019.
- N. Samusik, Z. Good, M. H. Spitzer, K. L. Davis, and G. P. Nolan. Automated mapping of phenotype space with single-cell data. *Nature methods*, 13(6):493, 2016.
- V. Saravanan, G. J. Berman, and S. J. Sober. Application of the hierarchical bootstrap to multi-level data in neuroscience. *BioRxiv*, page 819334, 2019.
- S. L. Smith, P.-J. Kindermans, C. Ying, and Q. V. Le. Don't decay the learning rate, increase the batch size. *arXiv preprint arXiv:1711.00489*, 2017.
- K. Sohn. Improved deep metric learning with multi-class n-pair loss objective. In *Advances in neural information processing systems*, pages 1857–1865, 2016.
- A. Srivastava, L. Valkov, C. Russell, M. U. Gutmann, and C. Sutton. Veegan: Reducing mode collapse in gans using implicit variational learning. In *Advances in Neural Information Processing Systems*, pages 3308–3318, 2017.
- G. J. Stephens, B. Johnson-Kerner, W. Bialek, and W. S. Ryu. Dimensionality and dynamics in the behavior of *c. elegans*. *PLoS Comput Biol*, 4(4):e1000028, 2008.
- G. J. Stephens, M. B. de Mesquita, W. S. Ryu, and W. Bialek. Emergence of long timescales and stereotyped behaviors in *caenorhabditis elegans*. *Proceedings of the National Academy of Sciences*, 108(18):7286–7289, 2011.
- S. Still and W. Bialek. How many clusters? an information-theoretic perspective. *Neural computation*, 16(12):2483–2506, 2004.
- J. R. Stowers, M. Hofbauer, R. Bastien, J. Griessner, P. Higgins, S. Farooqui, R. M. Fischer, K. Nowikovsky, W. Haubensak, I. D. Couzin, et al. Virtual reality for freely moving animals. *Nature methods*, 14(10):995, 2017.
- C. Stringer, M. Pachitariu, N. Steinmetz, M. Carandini, and K. D. Harris. High-dimensional geometry of population responses in visual cortex. *Nature*, 571(7765):361–365, 2019a.
- C. Stringer, M. Pachitariu, N. Steinmetz, C. B. Reddy, M. Carandini, and K. D. Harris. Spontaneous behaviors drive multidimensional, brain-wide activity. *cell*, 1(10):100, 2019b.

- D. Sussillo, R. Jozefowicz, L. Abbott, and C. Pandarinath. Lfads-latent factor analysis via dynamical systems. *arXiv preprint arXiv:1608.06315*, 2016.
- B. Szubert, J. E. Cole, C. Monaco, and I. Drozdov. Structure-preserving visualisation of high dimensional single-cell datasets. *Scientific reports*, 9(1):1–10, 2019.
- I. Tirosh, B. Izar, S. M. Prakadan, M. H. Wadsworth, D. Treacy, J. J. Trombetta, A. Rotem, C. Rodman, C. Lian, G. Murphy, et al. Dissecting the multicellular ecosystem of metastatic melanoma by single-cell rna-seq. *Science*, 352(6282):189–196, 2016.
- J. G. Todd, J. S. Kain, and B. L. de Bivort. Systematic exploration of unsupervised methods for mapping behavior. *Physical biology*, 14(1):015002, 2017.
- J. M. Tomczak and M. Welling. Vae with a vampprior. *arXiv preprint arXiv:1705.07120*, 2017.
- A. Van den Oord, N. Kalchbrenner, L. Espeholt, O. Vinyals, A. Graves, et al. Conditional image generation with pixelcnn decoders. In *Advances in neural information processing systems*, pages 4790–4798, 2016.
- A. Van Den Oord, O. Vinyals, et al. Neural discrete representation learning. In *Advances in Neural Information Processing Systems*, pages 6306–6315, 2017.
- L. van der Maaten. Learning a parametric embedding by preserving local structure. In *Artificial Intelligence and Statistics*, pages 384–391, 2009.
- L. van der Maaten. Accelerating t-sne using tree-based algorithms. *The Journal of Machine Learning Research*, 15(1):3221–3245, 2014.
- L. van der Maaten and G. Hinton. Visualizing data using t-sne. *Journal of machine learning research*, 9 (Nov):2579–2605, 2008.
- N. X. Vinh, J. Epps, and J. Bailey. Information theoretic measures for clusterings comparison: Variants, properties, normalization and correction for chance. *The Journal of Machine Learning Research*, 11: 2837–2854, 2010.
- M. Wang and D. Wang. Vmf-sne: Embedding for spherical data. In *2016 IEEE International Conference on Acoustics, Speech and Signal Processing (ICASSP)*, pages 2344–2348. IEEE, 2016.
- M. Waskom, O. Botvinnik, J. Ostblom, M. Gelbart, S. Lukauskas, P. Hobson, D. C. Gemperline, T. Augspurger, Y. Halchenko, J. B. Cole, J. Warmenhoven, J. de Ruyter, C. Pye, S. Hoyer, J. Vanderplas, S. Villalba, G. Kunter, E. Quintero, P. Bachant, M. Martin, K. Meyer, C. Swain, A. Miles, T. Brunner, D. O’Kane, T. Yarkoni, M. L. Williams, C. Evans, C. Fitzgerald, and Brian. mwaskom/seaborn: v0.10.1 (april 2020), Apr. 2020. URL <https://doi.org/10.5281/zenodo.3767070>.
- D. C. Wham, B. D. Ezray, and H. M. Hines. Measuring perceptual distance of organismal color pattern using the features of deep neural networks. *bioRxiv*, page 736306, 2019.
- A. B. Wiltschko, M. J. Johnson, G. Iurilli, R. E. Peterson, J. M. Katon, S. L. Pashkovski, V. E. Abaira, R. P. Adams, and S. R. Datta. Mapping sub-second structure in mouse behavior. *Neuron*, 88(6):1121–1135, 2015.
- J. Xie, R. Girshick, and A. Farhadi. Unsupervised deep embedding for clustering analysis. In *International conference on machine learning*, pages 478–487, 2016.
- L. Yang, N.-M. Cheung, J. Li, and J. Fang. Deep clustering by gaussian mixture variational autoencoders with graph embedding. In *Proceedings of the IEEE International Conference on Computer Vision*, pages 6440–6449, 2019.

Q. Zhang, J. Zhou, J. He, X. Cun, S. Zeng, and B. Zhang. A shell dataset, for shell features extraction and recognition. *Scientific data*, 6(1):1–9, 2019.

S. Zhao, J. Song, and S. Ermon. Infovae: Information maximizing variational autoencoders. *arXiv preprint arXiv:1706.02262*, 2017.